



Evaluation of operational model forecasts of aerosol transport using ceilometer network measurements

Ka Lok Chan^{1,2}, Matthias Wiegner¹, Harald Flentje³, Ina Mattis³, Frank Wagner^{3,4}, Josef Gasteiger⁵, and Alexander Geiß⁶

¹Meteorological Institute, Ludwig-Maximilians-Universität München, München, Germany

²Remote Sensing Technology Institute, German Aerospace Center (DLR), Oberpfaffenhofen, Germany

³Department of Research and Development, Meteorological Observatory Hohenpeissenberg, German Weather Service (DWD), Hohenpeissenberg, Germany

⁴Institute for Meteorology and Climate Research, Karlsruhe Institute of Technology, Eggenstein-Leopoldshafen, Germany

⁵Aerosol Physics and Environmental Physics, University of Vienna, Austria

⁶European Space Research and Technology Centre, European Space Agency, Netherlands

Correspondence: Ka Lok Chan (ka.chan@dlr.de)

Abstract. In this paper, we present a comparison of European Centre for Medium-Range Weather Forecast Integrated Forecast System (ECMWF-IFS) model simulation of aerosol backscatter profiles with measurements of the ceilometer network operated by the German weather service (DWD) over 1 year from September 2015 to August 2016. As the model output provides mass mixing ratios of different types of aerosol whereas the ceilometers don't, it is necessary to determine a common physical quantity for the comparison. We have chosen the attenuated backscatter β^* for this purpose. The β^* -profiles are calculated from the mass mixing ratios of the model output assuming the inherent aerosol microphysical properties. Comparison of the attenuated backscatter, averaged between an altitude from 0.2 km (typical overlap range of ceilometers) and 1 km, showed slightly larger values from the model.

To investigate possible reasons for the differences, we have examined the role of the hygroscopic growth of particles and the particle shape. Our results show that using a more recent particle growth model would result in a ~22 % reduction of particle backscatter for sea salt aerosols, corresponding to a 10 %-reduction of the total backscatter signal on average. Accounting for non-spherical dust particles in the model would reduce attenuated backscatter of dust particles by ~30 %. As the concentration of dust aerosol is in general very low in Germany, a significant effect on the total backscatter signal is restricted to dust episodes. In summary, consideration of both effects tend to improve the agreement between model and observations, but without leading to a perfect consistency.

In addition a case study was conducted to investigate the agreement of the spatiotemporal distribution of particles. It was found that for a dust episode in April 2016 the arrival time of the dust layer and its vertical extent very well agree between model and ceilometer measurements for several stations. However, due to the large set of parameters characterizing the aerosol distribution and the complexity of the ceilometer retrieval an automated and quantitative comparison scheme for β^* -profiles is still missing. Consequently, the representativeness of the case study remains open.



1 Introduction

Aerosols are an important constituent of the atmosphere playing a key role in the Earth's climate and weather system. They influence the Earth's radiation budget directly by absorbing and scattering of radiation and indirectly by providing nuclei for cloud condensation. The chemical and physical properties of aerosols depend on their composition and sources. In recent 5 decades, an increasing amount of anthropogenic aerosols is released into the atmosphere which makes it one of the largest uncertainties in assessments of climate change (IPCC, 2012). Numerous studies have been conducted in the recent decades to investigate the relationship between aerosols, air quality, weather and climate (Jones et al., 2001; Stier et al., 2005; Lohmann et al., 2007; Benedetti et al., 2009; Morcrette et al., 2009; Kazil et al., 2010; Wang et al., 2011; Zhang et al., 2012; Chan and Chan, 2017; Chan, 2017). These studies mostly rely on model simulations. However, atmospheric processing of aerosols 10 is quite complex, and their physical and chemical properties are highly variable, and cannot be easily characterized and parameterized. In addition, the emission sources of aerosols are not well estimated. Thus, simplifications and assumptions are usually required for numerical weather prediction (NWP) and assessments of climate change. As a consequence, validation of forecasts against observational data becomes increasingly important (e.g., Binietoglou et al., 2015; Cuevas et al., 2015; Curci et al., 2015; Siomos et al., 2017).

15 Quantitative range resolved aerosol parameters can be obtained from advanced lidar measurements. These lidar systems are very expensive and continuous operation is still an exception at the current state-of-the-art. On the other hand, ceilometers can be considered as simple single wavelength backscatter lidars with low energy consumption. Because they are eye-safe they can be operated continuously and fully automated, therefore making them suitable for setting up extended networks. In recent years, many of the synoptic observation stations have already been equipped with ceilometers and the number is still growing. 20 Although ceilometers were originally designed for cloud heights detection, recent studies show the ceilometers are also able to measure aerosol profiles (Flentje et al., 2010; Wiegner and Geiß, 2012; Madonna et al., 2015). If ceilometers are calibrated the primary output is the so-called attenuated backscatter β^* . This quantity can be converted to the particle backscatter coefficient β_p if the lidar ratio S_p is known. As β_p in the infrared spectral range is rather insensitive to errors of the lidar ratio this is typically not an issue.. In contrast, the derivation of the aerosol extinction coefficients α_p may be subject to large uncertainties. 25 As a consequence, β^* or β_p are candidates for validating aerosol profiles derived from NWP-models.

In this study, for the first time a comparison of aerosol profiles provided by the operational Integrated Forecast System of the European Centre for Medium-Range Weather Forecast (ECMWF-IFS) with long term measurements of the ceilometer network measurements operated by the German weather service (DWD) is presented. In section 2, the ceilometer data and the aerosol parameterizations of the model are described. As the model predicts mass mixing ratios of different types of aerosols whereas 30 the ceilometers provide backscatter-related quantities, the first step must be the selection of a common physical quantity for the comparison. It is described in section 3. The intercomparison discussed in section 4 comprises ceilometer measurements of one year (from 1. September 2015 to 31. August 2016) at 12 different stations in Germany and includes investigations of the importance of the numerical description of the hygroscopic growth of particles and the particle shape, and the agreement



of the spatiotemporal distribution of dust particles during a Saharan dust event. A summary and suggestions for further studies conclude the paper.

2 Basis of the intercomparison

The comparison of ‘aerosol profiles’ derived from weather forecast models and retrieved from ceilometer measurements suffers
5 from the fact that models and measurements do not provide the same physical quantity. In this section the output of the IFS and the ceilometers is described. This constitutes the basis for the determination of a common quantity for the intercomparison.

2.1 ECMWF-IFS: aerosol description

The European Centre for Medium-Range Weather Forecast Integrated Forecast System (ECMWF-IFS) is a comprehensive Earth-system model. The model is used for forecasts and analysis (Buizza et al., 1999; Rabier et al., 2000; Bechtold et al.,
10 Drusch et al., 2009; Dutra et al., 2013). In the framework of GEMS, aerosols were included as new prognostic variables into IFS (Morcrette et al., 2009; Benedetti et al., 2009). The parameterization of aerosol physics is mainly based on the concept of the LOA/LMD-Z model (Boucher et al., 2002; Reddy et al., 2005). The aerosol microphysics follows the sectional representation of the size distribution (e.g., Zhang et al., 1999; Mann et al., 2012). Tropospheric aerosols are introduced in the model including two natural types, sea salt and dust, and three other types with significant anthropogenic contribution, i.e.,
15 sulfate, organic matter and black carbon. Stratospheric and volcanic aerosols are not considered in the present version.

The emission of sea salt and dust is controlled by the wind speed at a height of 10 m. Following the findings of Engelstaedter and Washington (2007), it was suggested by Morcrette et al. (2008) to also consider the gustiness of the wind. The sources for the anthropogenic aerosols are taken from external emission inventories, i.e., the Emission Database for Global Atmospheric Research (EDGAR, 2013), the Global Fire Emission Database (GFED, van der Werf et al. (2010)) and the Speciated Particulate Emission Wizard (SPEW) were used in the simulation. A detailed description of the sources of aerosols can be found in Dentener et al. (2006).

The above mentioned five aerosol types are further subdivided: natural aerosols are categorized into three different size bins each, whereas carbonaceous aerosols are differentiated into hydrophobic and hydrophilic particles. Sulfur is presented in the model in two forms, sulfur dioxide (SO_2) and sulfate (SO_4), the former one was assumed in gas phase while the latter is
25 assumed in particulate phase. In total, the mass mixing ratios m of 11 different aerosol types (see Table 2) are introduced as prognostic variables in the model. It is provided with a temporal resolution of 3 hours. The horizontal resolution of the IFS model (version 41R1) is $1^\circ \times 1^\circ$, while the vertical dimension of the model is separated into 60 pressure-sigma levels. A more detailed description of the treatment of the aerosols can be found in Morcrette et al. (2009).

To determine the interaction between aerosols and radiation, the optical depth of each type is calculated for the short-wave
30 and long-wave spectral range. In this context also the change of the optical properties with relative humidity is considered. All calculations are based on the Mie theory even if the particles of a specific aerosol component are most likely non-spherical (e.g., dust).



The particle size distribution is assumed to be a lognormal distribution with three parameters: $\sigma_{g,i}$ as the ‘geometric standard deviation’, i.e., the width of the distribution, $r_{0,i}$ as the modal radius, and N_i as the total number concentration of particles of mode i . Thus, a size distribution (with r as the particle’s radius) consisting of k modes is described by Eq. 1

$$N(r) = \sum_{i=1}^k \frac{N_i}{\sqrt{2\pi} \cdot \ln \sigma_{gi} \cdot r} \cdot \exp \left\{ - \left(\frac{\ln r - \ln r_{0i}}{\sqrt{2} \cdot \ln \sigma_{gi}} \right)^2 \right\} \quad (1)$$

5 with normally $k \leq 3$.

In IFS, all aerosol types except sea salt are assumed to be a mono-modal lognormal distribution defined according to Eq. 1 ($k=1$). Only for sea salt, a bi-modal lognormal distribution is assumed ($k=2$). The parameters σ_g and r_0 characterizing each aerosol type are listed in Table 2. They are based on Reddy et al. (2005) and valid for dry particles.

For the sulfate, organic matter and black carbon aerosol type $\sigma_g = 2.0$ is selected and the modal radii r_0 are 0.0355, 0.0355
 10 and 0.0118 μm , respectively (Boucher and Anderson, 1995; Köpke et al., 1997). The microphysical properties of hydrophilic and hydrophobic carbonaceous aerosols are assumed to be the same.

Dust aerosols are also described by a mono-modal lognormal size distribution with $r_0 = 0.29 \mu\text{m}$ and $\sigma_g = 2.0$ (Guelle et al., 2000), but split into three size bins. The limits are 0.03 - 0.55 μm (fine mode), 0.55 - 0.9 μm (accumulation mode) and 0.9 - 20.0 μm (coarse mode), respectively. These boundaries are chosen so that approximately 10, 20 and 70 % of the total mass
 15 of the aerosols are in each of the size bins (Morcrette et al., 2009).

Sea salt aerosols as the second class of natural aerosols are also represented by three size bins. For dry sea salt aerosol, their limits are slightly different and set to 0.015 μm , 0.251 μm , 2.515 μm and 10.060 μm . In contrast to the dust aerosols, a bimodal lognormal with $r_0=0.1002 \mu\text{m}$ and 1.002 μm and $\sigma_g=1.9$ and 2.0 (O’Dowd et al., 1997) is assumed. The number concentrations N_1 and N_2 of the first and second mode are 70 and 3 cm^{-3} , respectively.

20 The refractive index of sea salt is assumed to be wavelength independent (Shettle and Fenn, 1979). For all other aerosol types a wavelength dependence is assumed and tabulated for 44 wavelengths between $\lambda=0.28 \mu\text{m}$ and $4.0 \mu\text{m}$, with values taken from Boucher and Anderson (1995); Köpke et al. (1997) and Dubovik et al. (2002). In Table 2 only values at 355 nm, 532 nm, 550 nm, 910 nm and 1064 nm are given, the latter two as they are the most relevant wavelengths for ceilometer applications, whereas the short wavelengths are relevant for aerosol lidar applications including satellite missions (CALIPSO, EarthCARE).

25 In case of hygroscopic growth of particles, their microphysical properties change. Typically this effect is parameterized by an increasing modal radius of the lognormal distribution, whereas the width of the distribution σ_g is assumed to remain unchanged. The latter approximation is certainly a simplification, but frequently used. In the IFS model, hygroscopic growth is considered for sulfate, hydrophilic organic matter and sea salt, see Fig. 1. It is parameterized by growth factors, defined as the ratio between the radius of the wet and dry particle (r/r_{dry}) and taken from the OPAC database (Hess et al., 1998). For sulfate and hydrophilic organic matter the same factors are used. Especially for a relative humidity above 70 % the growth is strong whereas no growth is assumed when the relative humidity is below 30 %. The refractive index n and density ϱ of wet particles is taken from a look up table with mixing rules following Hess et al. (1998).



To reduce computational time, the optical properties of hygroscopic aerosols are pre-calculated for 12 discrete relative humidity levels (0, 10, 20, 30, 40, 50, 60, 70, 80, 85, 90 and 95 %) and stored in a look-up table. It is important to note that sea salt aerosols are emitted and transported as wet aerosols in the model with properties equivalent to 80 % relative humidity. Subsequently, the model reported mass mixing ratios are converted back to dry aerosols by applying the inverse of the growth factor. The hygroscopic growth effect is then applied to the dry sea salt aerosols to determine the extinction and backscatter coefficient.

2.2 The ceilometer network

In recent years, DWD has equipped a number of synoptic observation stations with Lufft (previously Jenoptik) ceilometers (CHM15k) to establish a ceilometer network (www.dwd.de/ceilomap). By the end of 2016, 100 ceilometers are put into operation in Germany. The locations of the ceilometer sites are indicated in Fig. 2. The ceilometer network is still expanding in order to have a better spatial coverage. The ceilometers are eye-safe and fully-automated systems which allow unattended operation on a 24/7 basis (Wiegner et al., 2014). Thus they are especially suitable for monitoring aerosol layers (e.g., volcanic ash, see Flentje et al., 2010; Emeis et al., 2011), validation purposes of meteorological and chemistry transport models (see e.g. Baklanov et al., 2014), and are foreseen for data assimilation (e.g., Wang et al., 2014; Geisinger et al., 2017).

The CHM15k-ceilometer is equipped with a diode-pumped Nd:YAG-laser emitting laser pulses at 1064 nm. The typical pulse energy of the laser is about $8 \mu\text{J}$ with a pulse repetition frequency of 5 - 7 kHz. The laser beam with divergence of $<300 \mu\text{rad}$ is emitted off-axis to the receiving telescope with a field of view of $450 \mu\text{rad}$. Backscattered photons are collected by the telescope through a narrow band interference filter and measured by an avalanche photodiode running in photon counting mode. The received backscatter signals are stored in 1024 range bins with a resolution of 15 m, the temporal resolution is set to 15 s. The signals are corrected for incomplete overlap by a correction function provided by the manufacturer. As ceilometers are single-wavelength backscatter lidars the received signals follow the well known lidar equation. Calibration is required to retrieve quantitative results.

For the intercomparison of ceilometer measurements and modeled aerosol profiles we only consider sites within 20 km from a model grid point. This criterion results in a selection of 12 stations. Their location (latitude, longitude, altitude) together with their distance from the nearest IFS-grid point are summarized in Table 1.

3 Concept of intercomparison

As mentioned above, profiles of mass mixing ratios cannot directly be compared to ‘ceilometer profiles’. The latter can be expressed as particle backscatter coefficient $\beta_p(z)$ or as attenuated backscatter $\beta^*(z)$

$$\beta^*(z) = \beta(z) \exp \left\{ -2 \int_0^z \alpha(z') dz' \right\} \quad (2)$$



Table 1. Ceilometer sites within a distance of 20 km to the nearest IFS model grid point, altitude is given in meters above mean sea level, the distance to the nearest model grid point (in km) is given in the 5. column.

No.	Site	Latitude ($^{\circ}$ N)	Longitude ($^{\circ}$ E)	Altitude (m)	Distance (km)
1	Geisenheim	49.9866	7.9551	110	3.8
2	Wunsiedel	50.0316	11.9745	622	4.0
3	Elpersbüttel	54.0692	9.0105	3	7.8
4	Friesoythe	53.0500	7.9000	6	8.7
5	Boltenhagen	54.0027	11.1909	15	12.5
6	Pelzerhaken	54.0893	10.8773	1	12.7
7	Alfeld	51.9644	9.8072	144	14.1
8	Soltau	52.9605	9.7930	76	14.2
9	Bamberg	49.8743	10.9206	240	14.5
10	Gera	50.8813	12.1289	311	16.2
11	Görlitz	51.1633	14.9531	240	18.0
12	Offenbach	50.0894	8.7864	121	18.1

with z being the height, β and α the backscatter and the extinction coefficient, respectively. From the model results $\beta^*(z)$ and $\beta_p(z)$ can be calculated straight forward and the computational effort is comparable. Retrieval of both $\beta^*(z)$ and $\beta_p(z)$ from ceilometer measurements require the calibration of the ceilometer, i.e. the determination of the lidar constant C_L . The derivation of $\beta_p(z)$ requires furthermore an inversion of the signals (e.g. Klett, 1981; Fernald, 1984) relying on the assumption of a particle lidar ratio S_p , which is highly dependent on the aerosol composition. Consequently, additional uncertainties are introduced. It can be expected that the relative error of β_p is as good as approximately 15 % for specific Lufft ceilometers (Wiegner and Geiß, 2012) but can also exceed 30%. Note that water vapor absorption must be taken into account for ceilometers operating at 905 - 910 nm, otherwise β_p can be wrong by a factor of 2 (Wiegner and Gasteiger, 2015). Fortunately, this does not apply for the ceilometers of the DWD, but is relevant for other ceilometer networks.

For these reasons, and because weather services are in favor of the attenuated backscatter for intercomparisons, we chose $\beta^*(z)$ as the common quantity in this study for model evaluation. In this section, the procedures to derive attenuated backscatter from model simulations and ceilometer measurements are presented in detail.

3.1 Attenuated backscatter from model output

The model outputs consist of the mass mixing ratios $m_{p,i}$ of the 11 aerosol types. In a first step the mass mixing ratios of each aerosol type are converted to mass concentrations $c_{p,i}$ by multiplying with the air density ϱ_{air} as shown in Eq. (3).

$$c_{p,i}(z) = \varrho_{\text{air}}(z) m_{p,i}(z) \quad \text{for } i=1,2,\dots,11 \quad (3)$$



The particle extinction coefficient $\alpha_{p,i}$ of each aerosol type i is calculated using fundamental relations of scattering theory as shown in Eq. (4).

$$\alpha_{p,i}(z) = \pi \int_{r_1}^{r_2} r^2 Q_{\text{ext},i}(z) \frac{dN_i(r)}{dr} dr \quad (4)$$

where $Q_{\text{ext},i}$ is the extinction efficiency, and r_1 and r_2 the lower and upper limits of the size bin. The particle backscatter coefficient is defined in a similar way:

$$\beta_{p,i}(z) = \pi \int_{r_1}^{r_2} r^2 Q_{\text{bsc},i}(z) \frac{dN_i(r)}{dr} dr \quad (5)$$

with $Q_{\text{bsc},i}$ being the scattering efficiency multiplied with the phase function at 180° . For convenience it is common to use the lidar ratio $S_{p,i}$,

$$S_{p,i}(z) = \frac{\alpha_{p,i}(z)}{\beta_{p,i}(z)} \quad (6)$$

to calculate particle backscatter coefficients from extinction coefficients.

The extinction efficiencies and lidar ratios of each aerosol type are calculated applying the size distribution $dN(r)/dr$ and the refractive index n of the particles as assumed in the model, and by means of an appropriate scattering theory: for spherical particles the Mie theory is applied, for non-spherical particles a suite of approaches is available with the T-matrix (Mishchenko and Travis, 1998) being the most frequently used option. To be consistent with the current implementation of the aerosols in IFS we however rely on the Mie theory and use the Lorenz-Mie scattering algorithm (Mishchenko et al., 1999) even for non-spherical aerosol types as dust. In order to retrieve the optical properties of the 11 aerosol types integration was performed according to the given size bins, otherwise the upper limit was set to $r = 20 \mu\text{m}$. In case of hygroscopic growth of particles, their physical size, refractive index and density change according to the look up table mentioned above.

The conversion from the mass concentration to the extinction coefficient can now readily be achieved by the factor $\eta_{\alpha,i}$ (given e.g. in m^2/g)

$$\eta_{\alpha,i} = \frac{\alpha_{p,i}}{c_{p,i}} = \frac{3 \int_{r_1}^{r_2} r^2 Q_{\text{ext},i} (dN_i(r)/dr) dr}{4 \varrho_p \int_{r_1}^{r_2} r^3 (dN_i(r)/dr) dr} \quad (7)$$

in the radius interval from r_1 to r_2 . Finally, the extinction and backscatter coefficients of each aerosol type are determined – with consideration of Eq. (6) – according to

$$\begin{aligned} \alpha_{p,i} &= c_{p,i} \eta_{\alpha,i} \\ 25 \quad \beta_{p,i} &= c_{p,i} \left(\frac{\eta_{\alpha,i}}{S_{p,i}} \right) = c_{p,i} \eta_{\beta,i} \end{aligned} \quad (8)$$



Here, $\eta_{\beta,i}$ is the factor converting mass concentration to backscatter coefficient (of aerosol type i). The contribution of the air molecules is determined from the Rayleigh theory. We use the following approximation for the extinction coefficient α_m (in km^{-1})

$$\alpha_m(z, \lambda) = 8.022 \cdot 10^{-4} \varrho_{\text{air}}(z) \lambda^{-4.08}$$

5 with the air density given in kg/m^3 and the wavelength λ in μm . The profile of ϱ_{air} can be taken from the IFS output. The molecular lidar ratio S_m is known to be

$$S_m = \frac{\alpha_m}{\beta_m} \approx \frac{8\pi}{3}$$

For calculating $\beta^*(z)$, Eq. (2), we have to take all contributions into account, i.e., the (total) extinction coefficient α is

$$\alpha = \alpha_m + \sum_{i=1}^{11} \alpha_{p,i} + \alpha_w \quad (9)$$

10 and the (total) backscatter coefficient is

$$\beta = \beta_m + \sum_{i=1}^{11} \beta_{p,i} \quad (10)$$

Note, that the water vapor absorption coefficient α_w must only be considered in Eq. (9) if model results shall be compared to ceilometers operating in the spectral range around 905 - 910 nm (Wiegner and Gasteiger, 2015). This is e.g. the case if Vaisala-ceilometers are applied.

15 To increase the efficiency of the computations, $\eta_{\alpha,i}$ and $S_{p,i}$ are pre-calculated. An overview of aerosols in dry conditions for five different wavelengths is given in Table 2. The wavelengths correspond to Nd:YAG-lasers used for aerosol remote sensing (355 nm, 532 nm and 1064 nm), the widely used Vaisala ceilometers (910 nm), and the ‘typical wavelength’ for radiative transfer calculations in the shortwave spectral range (550 nm). Note, that the lidar ratios of some aerosol types differ from values published by, e.g., Groß et al. (2015) because of the limits of the particle size bins.

20 3.2 Attenuated backscatter from ceilometers

Attenuated backscatter β^* can be derived from the background corrected ceilometer signals P if the system has been calibrated, i.e., if the lidar constant C_L has been determined.

$$\beta^*(z) = \frac{P z^2}{C_L} \quad (11)$$



Table 2. Microphysical properties of dry aerosols assumed in the model.

Aerosol Type	Wavelength (λ , nm)	Density (ρ_p , g/cm ³)	Modal Radius (r_0 , μm)	Geometric Standard Deviation (σ_g)	Refractive Index (n)	Single Scattering Albedo (ω_0)	Specific Extinction Cross Section (σ_e , m ² /g)	Lidar Ratio (S_p , sr)
Sea Salt (bin 1) ^a	355	2.160	0.1002,1.0020 ^c	1.9,2,0 ^c	1.5156-0.0002i	1.00	6.37	56.9
Sea Salt (bin 2) ^a	355	2.160	0.1002,1.0020 ^c	1.9,2,0 ^c	1.5156-0.0002i	0.99	0.57	13.5
Sea Salt (bin 3) ^a	355	2.160	0.1002,1.0020 ^c	1.9,2,0 ^c	1.5156-0.0002i	0.97	0.16	18.8
Dust (bin 1) ^b	355	2.610	0.2900	2.0	1.4800-0.0025i	0.97	2.09	16.6
Dust (bin 2) ^b	355	2.610	0.2900	2.0	1.4800-0.0025i	0.94	0.99	19.2
Dust (bin 3) ^b	355	2.610	0.2900	2.0	1.4800-0.0025i	0.89	0.40	29.5
Organic Matter	355	1.769	0.0355	2.0	1.5280-0.0000i	1.00	5.69	35.5
Black Carbon	355	1.000	0.0118	2.0	1.7500-0.4500i	0.29	16.47	96.9
Sulfate	355	1.769	0.0355	2.0	1.5280-0.0000i	1.00	5.69	35.5
Sea Salt (bin 1) ^a	532	2.160	0.1002,1.0020 ^c	1.9,2,0 ^c	1.5156-0.0002i	1.00	3.56	76.0
Sea Salt (bin 2) ^a	532	2.160	0.1002,1.0020 ^c	1.9,2,0 ^c	1.5156-0.0002i	0.99	0.61	14.5
Sea Salt (bin 3) ^a	532	2.160	0.1002,1.0020 ^c	1.9,2,0 ^c	1.5156-0.0002i	0.98	0.17	15.7
Dust (bin 1) ^b	532	2.610	0.2900	2.0	1.4800-0.0018i	0.99	2.61	38.1
Dust (bin 2) ^b	532	2.610	0.2900	2.0	1.4800-0.0018i	0.96	0.88	9.5
Dust (bin 3) ^b	532	2.610	0.2900	2.0	1.4800-0.0018i	0.94	0.42	23.0
Organic Matter	532	1.769	0.0355	2.0	1.5227-0.0000i	1.00	3.25	42.3
Black Carbon	532	1.000	0.0118	2.0	1.7500-0.4500i	0.21	9.84	98.7
Sulfate	532	1.769	0.0355	2.0	1.5227-0.0000i	1.00	3.25	42.3
Sea Salt (bin 1) ^a	550	2.160	0.1002,1.0020 ^c	1.9,2,0 ^c	1.5156-0.0002i	1.00	3.33	74.0
Sea Salt (bin 2) ^a	550	2.160	0.1002,1.0020 ^c	1.9,2,0 ^c	1.5156-0.0002i	0.99	0.61	14.6
Sea Salt (bin 3) ^a	550	2.160	0.1002,1.0020 ^c	1.9,2,0 ^c	1.5156-0.0002i	0.98	0.17	15.4
Dust (bin 1) ^b	550	2.610	0.2900	2.0	1.4800-0.0016i	0.99	2.63	40.9
Dust (bin 2) ^b	550	2.610	0.2900	2.0	1.4800-0.0016i	0.97	0.87	9.9
Dust (bin 3) ^b	550	2.610	0.2900	2.0	1.4800-0.0016i	0.94	0.43	20.4
Organic Matter	550	1.769	0.0355	2.0	1.5220-0.0000i	1.00	3.07	42.5
Black Carbon	550	1.000	0.0118	2.0	1.7500-0.4500i	0.21	9.41	99.8
Sulfate	550	1.769	0.0355	2.0	1.5220-0.0000i	1.00	3.07	42.5
Sea Salt (bin 1) ^a	910	2.160	0.1002,1.0020 ^c	1.9,2,0 ^c	1.5156-0.0002i	1.00	0.89	36.0
Sea Salt (bin 2) ^a	910	2.160	0.1002,1.0020 ^c	1.9,2,0 ^c	1.5156-0.0002i	1.00	0.63	11.6
Sea Salt (bin 3) ^a	910	2.160	0.1002,1.0020 ^c	1.9,2,0 ^c	1.5156-0.0002i	0.99	0.17	15.9
Dust (bin 1) ^b	910	2.610	0.2900	2.0	1.4800-0.0006i	1.00	1.91	74.5
Dust (bin 2) ^b	910	2.610	0.2900	2.0	1.4800-0.0006i	1.00	1.54	35.2
Dust (bin 3) ^b	910	2.610	0.2900	2.0	1.4800-0.0006i	0.98	0.41	11.8
Organic Matter	910	1.769	0.0355	2.0	1.5114-0.0000i	1.00	1.12	37.5
Black Carbon	910	1.000	0.0118	2.0	1.7500-0.4500i	0.11	4.78	140.3
Sulfate	910	1.769	0.0355	2.0	1.5114-0.0000i	1.00	1.12	37.5
Sea Salt (bin 1) ^a	1064	2.160	0.1002,1.0020 ^c	1.9,2,0 ^c	1.5156-0.0002i	1.00	0.55	21.7
Sea Salt (bin 2) ^a	1064	2.160	0.1002,1.0020 ^c	1.9,2,0 ^c	1.5156-0.0002i	1.00	0.62	10.0
Sea Salt (bin 3) ^a	1064	2.160	0.1002,1.0020 ^c	1.9,2,0 ^c	1.5156-0.0002i	0.99	0.18	18.2
Dust (bin 1) ^b	1064	2.610	0.2900	2.0	1.4800-0.0006i	1.00	1.50	78.6
Dust (bin 2) ^b	1064	2.610	0.2900	2.0	1.4800-0.0006i	1.00	1.61	48.6
Dust (bin 3) ^b	1064	2.610	0.2900	2.0	1.4800-0.0006i	0.99	0.44	13.4
Organic Matter	1064	1.769	0.0355	2.0	1.5068-0.0000i	1.00	0.77	34.2
Black Carbon	1064	1.000	0.0118	2.0	1.7500-0.4500i	0.08	3.90	168.3
Sulfate	1064	1.769	0.0355	2.0	1.5068-0.0000i	1.00	0.77	34.2

^a Sea salt aerosols are represented in the model by three size bins with the bin limits set to 0.015-0.251 μm (bin 1), 0.251-2.515 μm (bin 2) and 2.515-10.060 μm (bin 3).

^b Dust aerosols are represented in the model by three size bins which the bin limits are set to 0.03-0.55 μm (bin 1), 0.55-0.90 μm (bin 2) and 0.90-20.00 μm (bin 3).

^c A bimodal lognormal size distribution is assumed for sea salt aerosols, with $r_0=1.002 \mu\text{m}$ and $1.002 \mu\text{m}$ and $\sigma_g=1.9$ and 2.0. The number concentrations N_1 and N_2 of the first and second mode are 70 and 3 cm^{-3} , respectively.

Note that density of hydrophilic aerosol changes with hygroscopic growth of particle.

It should be emphasized that C_L can vary with time (e.g. caused by aging of components, or temperature drifts). However, such changes are typically slow.

The calibration of the ceilometers of the network is performed routinely by the DWD in a fully automated procedure. The calibration relies on the Rayleigh method (Barrett and Ben-Dov, 1967). This is feasible under clear sky conditions and stable aerosol distributions, thus, the applicability depends on the measurement site. In order to avoid adverse influences caused by background sun light, only night time data are used for the calibration. The calibration is based on data averaged over 1 - 3 hours, and only one period is selected per night. Meteorological data used for the Rayleigh calibration are taken from



the joint product of the National Centers for Environmental Prediction (NCEP) and the National Center for Atmospheric Research (NCAR) reanalysis data (Kalnay et al., 1996). The derived lidar constants C_L are first cleaned for outliers and then smoothed with a 30 days running mean. Lidar constants outside 1.5 times of the 25 to 75 percentile range of a 30 days-period are considered as outliers. The smoothed C_L are finally interpolated to hourly values to be used in Eq. 11. The calibration 5 routine implemented in the DWD automatic calibration is based on the ToProf E-Profile Rayleigh calibration routine provided by MeteoSwiss. Then, attenuated backscatter β^* profiles are derived in steps of three hours, by averaging cloud free data within 30 minutes each before and after the corresponding model time. Longer averages are desirable in view of a better signal to noise ratio but are critical during day time when the aerosol distribution is rapidly changing in time. In cases of rain, snowfall, fog and low level clouds (below 2 km), the data are excluded from the evaluation. The corresponding information is taken from 10 the ‘sky-condition-index’ and ‘cloud-base-height’ provided by the proprietary software of the ceilometer.

The accuracy of the retrieved β^* linearly depends on the accuracy of the calibration constant C_L which can be quite different for different sites and instruments.

4 Results and discussions

There are many options to discuss the agreement of β^* -profiles from model calculations and ceilometer measurements: criteria 15 include the comparison of absolute values of β^* , the general ‘shape’ of the profiles, the vertical extent of the mixing layer and elevated layers, the vertical structure of the aerosol distribution within the mixing layer, and more. A general philosophy on a ranking of different criteria has not yet been developed, e.g., there is no common agreement how to rate profiles when the modeled altitude of an elevated layer is consistent with measurements but the absolute values of β^* are (quite) different. The reason is that the attenuated backscatter of e.g. elevated Saharan dust or volcanic ash layers does not only depend on the 20 aerosol properties of that layer, but is also influenced by the extinction below that layer. In order to minimize this influence and to consider that part of the atmosphere where most of the aerosols typically reside, we focus in this paper on β^* of the lowermost part of the troposphere excluding the range of incomplete overlap. All ceilometer data have undergone an individual overlap correction provided by the manufacturer that makes it possible to use profiles for aerosol remote sensing from above approximately 200 m. In the following, we compare β^* averaged from the typical height of a ‘reliable overlap correction’ (set 25 to 200 m for all instruments) to 1 km above ground, henceforward referred to as ‘near surface average’ $\overline{\beta_{ns}^*}$. An additional approach of comparison is discussed in Sect. 4.2.

Our investigation is based on measurements from 1. September 2015 until 31. August 2016. Attenuated backscatter profiles are derived from the model results for every 3 hours following the procedure outlined in section 3.1. Ceilometer data are averaged over 1 hour around the model time and only profiles are considered that reach at least a height of 2 km above the 30 ground, i.e., profiles contaminated by low level clouds and precipitation are excluded. As a consequence, averages consider 240 ceilometer profiles at maximum.



4.1 Comparison of near surface attenuated backscatter

For an overview the complete time series of the model simulation and ceilometer observation of the near surface attenuated backscatter $\overline{\beta_{ns}^*}$ over Elpersbüttel is shown in Fig. 3. This site has been chosen as it is one of the closest to the corresponding model grid point (only 7.8 km south west of the ceilometer site, see Table 1) and the orography around the measurement site 5 is quite flat. For Elpersbüttel we found 1305 cases out of 2920 (365×8) when intercomparisons could take place. The number of cases varies in a range from 900 (Wunsiedel) to 1763 (Boltenhagen). Results show that the model and ceilometer data both show a similar temporal development with larger $\overline{\beta_{ns}^*}$ during winter and spring. Note, that due to cloudy weather during winter 10 the number of useful ceilometer measurements is reduced compared to summer. In cases of low aerosol load there is a general agreement of both data sets. However, when episodes of large values of $\overline{\beta_{ns}^*}$ are modeled they typically exceed the observed ones by a factor of two or more. This is e.g. the case in December 2015, beginning of February 2016 and April 2016. The 15 reasons for this overestimate must remain speculative - maybe it is due to erroneous assumptions of the aerosol emission or meteorological data. On the other hand the annual mean derived from the model $\overline{\beta_{ns}^*} = 1.35 \times 10^{-3} \text{ km}^{-1} \text{ sr}^{-1}$ agrees very well with the corresponding value of $\overline{\beta_{ns}^*} = 1.31 \times 10^{-3} \text{ km}^{-1} \text{ sr}^{-1}$ from the ceilometer observations at Elpersbüttel. For most 20 of the other sites listed in Table 1, the model obtains higher values than the ceilometer measurements by $\sim 20\%$ on annual average. This is still a considerably good agreement. Few exceptions are Bamberg, Boltenhagen and Gera where the model predicts much lower values than observed. The largest difference of a factor of 1.8 is found for Gera with measurement and model mean values of $\overline{\beta_{ns}^*} = 1.85 \times 10^{-3} \text{ km}^{-1} \text{ sr}^{-1}$ and $\overline{\beta_{ns}^*} = 9.99 \times 10^{-4} \text{ km}^{-1} \text{ sr}^{-1}$, respectively. These stations show larger impacts from the local emissions as they are situated close to the cities. The discrepancy between ceilometer observations and model predictions over these three sites is mainly due to the differences in the spatial coverage. As the model resolution is 25 rather coarse ($1^\circ \times 1^\circ$) and therefore the model resulting in an underestimation of the aerosol concentrations over cities due to the averaging effect over large grid cell.

For a more detailed analysis we have calculated the differences Δ between modelled and ceilometer derived $\overline{\beta_{ns}^*}$ with

$$\Delta = \overline{\beta_{ns}^*}(\text{mod}) - \overline{\beta_{ns}^*}(\text{obs}) \quad (12)$$

for Elpersbüttel (see Fig. 4a). The size of the markers is proportional to the number of ceilometer measurements (up to 240) 25 available for each individual intercomparison. The standard deviation σ of the difference is $\sigma = 1.89 \times 10^{-3} \text{ km}^{-1} \text{ sr}^{-1}$, i.e. quite large compared to the model mean value of $\overline{\beta_{ns}^*} = 1.35 \times 10^{-3} \text{ km}^{-1} \text{ sr}^{-1}$. Data points with $\Delta > 3\sigma$ are considered as outliers (marked in red in Fig. 4a) and filtered out in the subsequent analysis. Remaining data are then used to recalculate the standard deviation ($\sigma = 1.20 \times 10^{-3} \text{ km}^{-1} \text{ sr}^{-1}$). The recalculated standard deviation is marked on Fig. 4a.

To better understand possible reasons for these differences we have looked into the contribution of different aerosol types. 30 Their relative contributions to $\overline{\beta_{ns}^*}$ as calculated from the model for Elpersbüttel reveal that sea salt is by far the dominating contributor with 61 % (annual mean). Sulfate contributes with 29 % to the near surface attenuated backscatter, while organic matter (4 %), dust (3 %) and black carbon (2 %) only show minor contributions. We have re-calculated these contributions



separately for two classes: cases of ‘good’ agreement ($\Delta < \sigma$) are shown in Fig. 4b, whereas cases of ‘bad’ agreement ($\Delta > \sigma$) are shown in Fig. 4c. Each aerosol type is color coded as indicated in the legend.

From Fig. 4b it is immediately visible that for the good agreement sea salt is again the dominating aerosol type: its contribution ranges between 32 % (May 2016) and 85 % (December 2015) with an annual average of 51 %. The second important 5 contributor are sulfate aerosols (32 % on average) whereas all other types are in the range of a few percent each. Thus, cases of good agreement coincide with a sea salt contribution lower than the mean. Consequently, the contribution of sea salt is above the average when the differences between model and measurement are large ($\Delta > \sigma$). From Fig. 4c a mean relative contribution of sea salt of 74 % for the ‘bad’ agreement is derived. This suggests that the ceilometer and model discrepancy increases with increasing sea salt contribution.

10 Scatter plots of the ceilometer and the model derived near surface attenuated backscatter for the 12 sites are shown in Fig. 5. The color code represents the relative contribution of sea salt to $\overline{\beta_{ns}^*}$. For most sites red dots are predominant, indicating the high contribution of sea salt. This phenomenon has already been discussed in case of Elpersbüttel. When the sea salt contribution is rather low, the model typically shows lower $\overline{\beta_{ns}^*}$ than the ceilometer retrieval. This is probably due to local emissions which are not well resolved by the model but captured by the ceilometer measurements. The total least squares regression line is 15 based only on intercomparisons when at least 120 ceilometer profiles could be evaluated. The regression is virtually unchanged when the number of valid ceilometer profiles is used as a weight. The slope of the regression line is larger than 1 for all sites, indicating that the model in general results in larger $\overline{\beta_{ns}^*}$. In particular this is true when the contribution of sea salt is high, e.g. for Friesoythe, Geisenheim and Offenbach. Note, that the latter two stations are far from the coast so that the large sea salt contribution seems to be unrealistic. Pearson’s correlation coefficient R ranges between $R=0.12$ for Bamberg and $R=0.80$ for 20 Elpersbüttel with no clear dependence on the distance between the model grid point and the ceilometer site.

Reasons for the disagreement can be manifold: One possibility is that the backscatter per unit mass of sea salt is too large in the model. As the optical properties of sea salt critically depend on the hygroscopic growth we have investigated to which extent this effect might explain the observed differences (see section 4.1.1). Another reason could be that the modeled sea salt concentration is generally overestimated, and that it should partly be replaced by an aerosol type that is less effectively 25 backscattering. A discussion of this topic is however beyond the scope of this paper.

4.1.1 Influence of hygroscopic growth

Water uptake by particles has a significant impact on their optical properties as particles can change in size, chemical composition and refractive index depending on the ambient relative humidity. The assumptions made for their hygroscopic growth have a significant effect on the simulation of ceilometer measurements from the model output. For this reason, we examine the 30 hygroscopic growth effect on the conversion factor η_β for sea salt (see Eq. 8) as the dominating aerosol species (in terms of backscatter) according to the IFS output. We compare two approaches, being aware that more are existing (e.g., Chin et al., 2002): the growth model used in the IFS model (based on OPAC, Hess et al. (1998)) and a more recent approach (Swietlicki et al., 2008), see Fig. 1. The latter was reported to better match experimental data (Zieger et al., 2013). Compared to OPAC it shows a less pronounced particle growth with relative humidity. The corresponding conversion factors $\eta_{\beta,ss}$ of sea salt are



shown in Fig. 6a for comparison. Results referring to the three different size bins of the particle model are shown in blue, green and red, respectively. The ratios of the conversion factors from the two approximations ($\eta_{\beta,ss}^{(swie)} / \eta_{\beta,ss}^{(opac)}$) are shown in Fig. 6b. The conversion factors based on Swietlicki et al. (2008) are on average smaller than those based on the OPAC database, however, differently for each size bin and depending on the relative humidity. By comparing data calculated with the OPAC 5 database, the alternative set of conversion factors $\eta_{\beta,ss}^{(swie)}$ typically reduce backscatter coefficients by a factor between 0.6 and 0.8, with an average of 0.78. Consequently, the change of $\overline{\beta_{ns}^*}$ when replacing the hygroscopic growth function can be significant and quite variable. Taking into account that sea salt particles in general contribute more than 50 % to the attenuated 10 backscatter over Germany, overestimating the conversion factor by 22 % on average would already contribute up to an error of more than 10 % of the total backscatter signal. It should be emphasized that – as a side effect – an overestimated hygroscopic growth of sea salt leads to an increased aerosol extinction coefficient in the mixing layer. Consequently attenuated backscatter is reduced at higher altitudes, making the identification of elevated aerosol layers in principle more difficult.

In order to quantify the effect of a changed hygroscopic growth we recalculate β^* from modeled mixing ratios by using the 5 alternative set of conversion factors (Swietlicki et al., 2008) and compare it to ceilometer observations. Analogously to Fig. 5 scatter plots of the ceilometer derived and modeled $\overline{\beta_{ns}^*}$ for the 12 sites are shown in Fig. 7. Compared to the original model 15 assumptions, modeled attenuated backscatter shows a slightly better agreement with the ceilometer measurements. Although the correlation coefficients between ceilometer and model $\overline{\beta_{ns}^*}$ are nearly unchanged, the slope of the regression lines is on average reduced by ~30 % and agrees better with the 1 to 1 reference line. This effect is more obvious for sites dominated by sea salt aerosols in Northern Germany, e.g. Boltenhagen, Elpersbüttel, Pelzerhaken and Soltau, while sites with lower sea salt contributions are nearly unaffected, e.g., Görlitz and Wunsiedel. The result indicates that the updated hygroscopic growth 20 function leads to a better agreement between model simulations and measurements. However, the model is still overestimating $\overline{\beta_{ns}^*}$, indicating that the assumption of a reduced hygroscopic growth alone cannot fully explain the mismatch between model and observations.

4.1.2 Influence of particle shape

Besides of the hygroscopic growth of hydrophilic aerosols, the shape of particles also plays an important role for the optical 25 properties of the particles. Mineral dust particles are typically non-spherical, however, they are often - e.g. in the IFS model - considered as spherical particles in order to simplify the computation. To quantify the influence of the shape-effect of mineral dust particles, we compared modeled β_p and β^* using either the spherical or the non-spherical assumption. In case of non-spherical mineral dust particles, spheroids with an aspect ratio distribution measured by Kandler et al. (2009) and successfully applied in the closure experiment of optical properties of dust by Wiegner et al. (2009) in the framework of SAMUM, are 30 assumed in T-Matrix calculations (Waterman, 1971; Mishchenko and Travis, 1998). Table 3 shows the comparison of optical properties of dust particles: it can be seen that non-spherical particles have a significantly larger lidar ratio S_p whereas the specific extinction cross section σ_e^* is nearly unchanged. As a result β_p is reduced by 15 - 45 % if non-sphericity is considered, whereas the effect on the extinction is small.



Table 3. Comparison of selected optical properties at 1064 nm of mineral dust particles assuming spherical and non-spherical shapes. Spheroid particles with an aspect ratio distribution measured by Kandler et al. (2009) is assumed for non-spherical dust particles.

species	spherical		non-spherical		difference in particle backscatter ($\Delta \beta_p$, %)
	specific extinction cross section (σ_e^* , m ² /g)	lidar ratio (S_p , sr)	specific extinction cross section (σ_e^* , m ² /g)	lidar ratio (S_p , sr)	
Dust (0.03 - 0.55 μm)	1.496	78.6	1.449	89.0	-14.4
Dust (0.55 - 0.90 μm)	1.611	48.6	1.602	69.4	-30.3
Dust (0.90 - 20.0 μm)	0.445	13.4	0.495	26.6	-44.0

We have also investigated the influence of the treatment of particle shape on the mass to backscatter conversion factors η_β of the three dust size bins. For demonstration one 1-hour profile from a dust episode (3. April 2016, 18:00 UTC, see also next section) is discussed in detail. Attenuated backscatter profiles are shown in Fig. 8a. Ceilometer measurements with the original vertical resolution of 15 m are shown in light red, whereas the bold red line shows the ceilometer profile re-sampled for 5 the model's resolution. Profiles derived from the model output are given in blue and green, respectively, for the spherical and non-spherical assumption. Fig. 8a clearly demonstrates that the observed decrease of β^* in the height range between ~ 1.1 km and ~ 3.5 km is very well reproduced by the model simulations, independent of the numerical treatment of the particle shape. However, the absolute values agree somewhat better if non-sphericity is assumed. This improvement is most pronounced in the lowermost layer where dust is the dominating contributor: here the overestimate of β^* with respect to the ceilometer retrievals 10 is clearly reduced but still in the order of up to a factor of 3 which also implies that the model is overestimating the dust concentration during this episode. Note, that the increased attenuated backscatter at ~ 8 km as observed by the ceilometer is due to the presence of clouds. The modeled β_p of the different aerosol types is shown in Fig. 8b and Fig. 8c, assuming either sphericity or non-sphericity of dust particles. Below 3 km dust is by far the dominating aerosol type. As can be expected from 15 Table 3 β_p of the dust component is reduced by 15 - 45 % for the three size bins when non-sphericity is considered. For the profile shown this leads to a reduction of ~ 33 % of the total particle backscatter coefficient and a better agreement with the observations as was shown in the left panel. On the other hand, differences of the aerosol optical depth are negligible (less than 1 %) even during the dust episode. As the concentration of mineral dust aerosol is in general very low in Germany, introducing non-spherical mineral dust in the IFS-model only has a minor impact on the annual average. However, in case of dust events 20 non-sphericity should be considered to obtain the best possible agreement. This also holds for volcanic ash layers which are not yet included in the model.



4.2 Comparison of the spatiotemporal distribution

The focus of the previous section was on the agreement of the attenuated backscatter vertically averaged over the lower troposphere. In the following case study of a dust event we briefly want to outline further options to compare model predictions and measurements of the ceilometer network.

- 5 Dust particles are typically a minor contributor to the aerosol abundance in Germany. On average, it contributes less than 5 % of the total attenuated backscatter according to the IFS model. However, episodes with high concentrations are observed in Germany caused by long range transport of Saharan dust towards Europe (Ansmann et al., 2003; Stut et al., 2009; Müller et al., 2009). From September 2015 to August 2016 there were two major dust episodes affecting Germany as a whole: in December 2015 and April 2016. The temporal development of the latter from 2. April 2016 to 4. April 2016 is shown in Fig. 9
10 in terms of the modeled dust concentration (in $\mu\text{g}/\text{m}^3$), averaged over the lowermost kilometer of the troposphere: the dust layer approached Germany from southwest by 2. April and covered large parts of Germany when moving eastwards (3. and 4. April). The episode came to an end on 5. April when only Austria was still affected (not shown). During this event all 12 sites show peak dust contributions of over 50 % of the total $\overline{\beta_{ns}^*}$.

Again we choose Elpersbüttel as an example for the agreement between model and observations. Fig. 10 shows the time-height cross section of the attenuated backscatter of the ceilometer and the corresponding profiles calculated from the model output. Here we treat dust particles as spheres to be consistent with the IFS-model.

From the ceilometer measurements it seems that the dust arrived in Elpersbüttel at 18:00 UTC at the latest; however, due to the presence of low level clouds the arrival could be up to 4 hours earlier. Pronounced signatures of enhanced backscatter can be observed up to almost 7 km (see Fig. 10a). This is in excellent agreement with the modeled profiles for 18:00 UTC
20 and 21:00 UTC: the aerosol layer is clearly visible up to 6 km and 7 km, respectively; even the pronounced aerosol layer up to approximately 1.5 km is resolved. The absolute values of β^* are similar with largest differences in the lowermost kilometer. For the time period before 18:00 UTC the model shows a slightly enhanced β^* at altitudes above 3 km, that is not visible in the measurements. On the other hand the vertical extent of the mixing layer is very well reproduced by the model.

The temporal development of the attenuated backscatter over Elpersbüttel on 3. April 2016 is shown in Fig. 11. The ceilometer measurements show an pronounced elevated aerosol layer which is clearly separated from the surface aerosol layer before 04:00 UTC. It can be assumed that the lower layer primarily contains locally produced particles (typically the mixing layer height is lower than 1.5 km in spring in Germany) whereas the upper layer is Saharan dust. This is plausible but cannot be proven from data of a single wavelength backscatter ceilometer without depolarization channel. Moreover, from the ceilometer data it is not possible to determine the top of the aerosol layer due to clouds, nevertheless measurements at 01:00 UTC
30 and 03:00 UTC suggest that aerosols were present up to approximately 4 km for the first few hours of the night. The model shows large values of β^* up to 4 km until 09:00 UTC with dust as the dominating contributor. For the second half of the day the dust layer is confined to the lowermost 3 km according to the model (see Fig. 8). Again, the general agreement of the vertical extent of the aerosol layer is very good. However, it must remain open whether the thin layer at 6 - 7 km, visible in the modeled β^* -profiles at 09:00 UTC and 12:00 UTC is real or not. The measurement range of the ceilometer is blocked by



clouds in 3 km altitude, and even under cloudfree conditions the ceilometer might have missed that layer due to the high solar background illumination around noon. In spite of the generally good agreement of the profiles, the absolute values of β^* below 1 km sometimes differ considerably as has been already demonstrated in Fig. 8.

The situation of the last day of the event is shown in Fig. 12. From the ceilometer observations it can be concluded that 5 the elevated aerosol layer disappears at around 19:00 UTC. Prior to this, visual inspection of β^* suggest that dust is present up to at least 2 km. Again, the upper boundary cannot be detected before 08:00 UTC due to low level clouds. According to the model prediction the dust event should persist over Elpersbüttel until 18:00 UTC or 21:00 UTC of 4. April 2016. This is in perfect agreement with the observations. However, further validation of the vertical extent is hardly possible due to the above mentioned clouds. It is likely that the large attenuated backscatter in the elevated layer until about 18:00 - 20:00 UTC is 10 mainly caused by dust. However, this cannot be clarified by the ceilometer measurements, as no depolarization ratios can be determined.

The overall good agreement between model and observation is confirmed for other sites in Germany. For example, the ceilometer at Soltau, 130 km southeast of Elpersbüttel, observes the dust layer the first time on 2. April, 17:00 UTC, between 3 km and 7 km - in agreement with the model predictions. This also holds for Pelzerhaken (120 km east of Elpersbüttel) 15 where the ceilometer measurements suggests an arrival of the layer by shortly before 22:00 UTC whereas the model results indicate a pronounced dust contribution the first time by 21:00 UTC. In central Germany (Offenbach) the arrival time is earlier, approximately at 09:00 UTC according to both model and observations. The upper boundary of the layer is somewhat larger according to the model (6 km vs. 4 km from the observations), however, the ceilometer measurements are subject to high solar background limiting their vertical range. For 3. April the dust event was detected at all stations. In some cases, e.g. Offenbach, 20 the vertical extent of the layer could however not be validated due to low and mid-level clouds.

Taking the underlying limitations of remote sensing with a ceilometer into account we conclude that observations and model match very well: this includes the presence of the dust layer, the vertical extent of the layer and – to a lesser extent – also the absolute values of β^* . Discrepancies in the lower part of the troposphere might partly originate from local sources of particles, that are not resolved by the model. The discrimination of different aerosol types is in principle not possible with current state-of-the-art ceilometer networks, and it is not possible to penetrate optically thick clouds anyhow. Moreover, this case study 25 suggests that an automated numerical scheme to quantitatively intercompare modeled and measured β^* -profiles must be very complex.

5 Summary and Conclusions

In this paper, we have compared attenuated backscatter (β^*) profiles calculated from model simulation of the European Centre 30 for Medium-Range Weather Forecast Integrated Forecast System (ECMWF-IFS) and ceilometer network measurements operated by the German weather service (DWD) over one year from September 2015 to August 2016. The model includes prognostic equations for the mass mixing ratio of 11 different types of aerosols. In terms of backscatter coefficient β_p , sea salt is the dominating type (more than 50 %) for virtually all sites over Germany. If ceilometers are properly calibrated, attenuated



backscatter can be derived. This quantity was chosen as the common physical quantity for the intercomparison as it is independent to the assumption of a lidar ratio in the ceilometer retrieval. The β^* -profiles are calculated from the mass mixing ratios of the model according to the inherent aerosol microphysical properties. Ceilometers are used for intercomparison when a model grid point could be found within 20 km. In total, 12 sites fulfill this criterion. Comparison of the attenuated backscatter averaged over the lowest part of the atmosphere ($\overline{\beta_{ns}^*}$, from the mean overlap range of ceilometers of 0.2 km to 1 km above ground) shows similar annual averages, however, there are several cases where the modeled $\overline{\beta_{ns}^*}$ exceeds the ceilometer measurements.

To find reasons for the disagreement, we have examined the role of hygroscopic growth of particles and the role of particle shape. We have calculated β^* substituting the current hygroscopic growth function of sea salt particles (based on OPAC) by a more recent function (Swietlicki et al., 2008). Our calculations show that this change results in a significant reduction of particle backscatter of sea salt. As sea salt is the major contributor to the particle backscatter coefficient, the effect on the modeled attenuated backscatter is significant and in the order of 10 % on average. As a consequence implementing a more recent hygroscopic growth function leads to a better agreement between ceilometer measurements and model. The importance of the consideration of the particle shape in case of mineral dust particles is investigated separately. Instead of the currently used assumption of spherical particles, we apply the T-matrix method for spheroids with a measured aspect ratio distribution. Application of the T-matrix method reduces β_p of dust by 15 - 45 %. A case study of a dust episode for one of the 12 selected sites, Elpersbüttel, shows a better agreement between model and ceilometer measurement when applying optical properties of non-spherical dust particles. As on average the concentration of dust aerosol is very low in Germany, a significant effect on the total attenuated backscatter is however confined to dust episodes.

Finally we have investigated the ‘agreement’ between model and observations in case of a dust event. In this context we understand ‘agreement’ as the same time period of the event (appearance, dissolution) and the same vertical extent of the dust layer. The case study shows a quite good general qualitative agreement but also highlights the inherent problems of ceilometer measurements when low clouds are present, and missing information for aerosol typing. Moreover, there is a certain degree of ambiguity in the definition of the ‘beginning’ and ‘end’ of a dust event.

From our study we conclude that intercomparisons of aerosol profiles derived from models and measurements should be extended in several ways:

1. A better model resolution is desirable so that more cases can be found where the distance between a model grid point and a ceilometer site is a few kilometers only. This would strengthen the conclusions. A recent update of the IFS does indeed provide a resolution of 0.5° , and DWD is continuously extending the ceilometer network (120 by the end of 2017). Moreover, attenuated backscatter is included in the model’s output since 26. September 2016 offering new options for intercomparisons.
2. Intercomparisons should take advantage of as many profile information as possible: not only the vertical profile of β^* , but also the agreement in terms of altitude, extent, temporal development and mean particle backscatter β_p of extended/elevated aerosol layers should be addressed. In this paper we have discussed only one dust event for demonstration purposes and found good agreement with respect to the vertical extent of the layer and its temporal development.



Whether this finding is valid in general must be investigated in further studies. This effort might include the development of automated algorithms for layer detection and particle characterization. Due to their unprecedented spatial coverage ceilometer networks may constitute the observational backbone, nevertheless the combination with a small set of advanced lidar systems should be envisaged.

- 5 3. Investigation of the influence of meteorological fields and the chemical formalism of the model, e.g. emission schemes, on the aerosol composition and the corresponding attenuated backscatter profiles should be encouraged.

Code and data availability. The source code of the ECMWF IFS model is not available for public as it is an operational model running on routine bases. The ECMWF IFS model simulation results are available to the meteorological offices of the member states of ECMWF. The raw data of the ceilometer instruments are available on request from the data originator DWD (datenservice@dwd.de). The database of 10 aerosol optical properties used in this study is available on request from the corresponding author (ka.chan@dlr.de).

Competing interests. The authors declare that they have no conflict of interest.

Acknowledgements. We thank Maxime Hervo and his colleagues at MeteoSwiss for the provision of the ToProf E-Profile Rayleigh calibration routine. This work has been partially supported by the European Center for Medium Weather Forecast (ECMWF) through its main contractor Royal Netherlands Meteorological Institute (KNMI) and KNMI's subcontractor German Weather Service (DWD) in the context of the 15 Copernicus Atmosphere Monitoring Service (CAMS). The work described in this paper was partially supported by the Marie Curie Initial Training Network of the European Seventh Framework Programme (Grant No. 607905) and the European Cooperation in Science and Technology (COST) action 'TOPROF' of the European Union's Horizon 2020 programme (Project No. ES1303). Josef Gasteiger has received funding from the European Research Council (ERC) under the European Union's Horizon 2020 research and innovation programme (Grant No. 640458, A-LIFE).



References

- Ansmann, A., Bösenberg, J., Chaikovsky, A., Comerón, A., Eckhardt, S., Eixmann, R., Freudenthaler, V., Ginoux, P., Komguem, L., Linné, H., Márquez, M. n. L., Matthias, V., Mattis, I., Mitev, V., Müller, D., Music, S., Nickovic, S., Pelon, J., Sauvage, L., Sobolewsky, P., Srivastava, M. K., Stohl, A., Torres, O., Vaughan, G., Wandinger, U., and Wiegner, M.: Long-range transport of Saharan dust to northern Europe: The 11–16 October 2001 outbreak observed with EARLINET, *Journal of Geophysical Research: Atmospheres*, 108, <https://doi.org/10.1029/2003JD003757>, <http://dx.doi.org/10.1029/2003JD003757>, 4783, 2003.
- Baklanov, A., Schlünzen, K., Suppan, P., Baldasano, J., Brunner, D., Aksoyoglu, S., Carmichael, G., Douros, J., Flemming, J., Forkel, R., Galmarini, S., Gauss, M., Grell, G., Hirtl, M., Joffre, S., Jorba, O., Kaas, E., Kaasik, M., Kallos, G., Kong, X., Korsholm, U., Kurganskiy, A., Kushta, J., Lohmann, U., Mahura, A., Manders-Groot, A., Maurizi, A., Moussiopoulos, N., Rao, S. T., Savage, N., Seigneur, C., Sokhi, R. S., Solazzo, E., Solomos, S., Sørensen, B., Tsegas, G., Vignati, E., Vogel, B., and Zhang, Y.: Online coupled regional meteorology chemistry models in Europe: current status and prospects, *Atmospheric Chemistry and Physics*, 14, 317–398, <https://doi.org/10.5194/acp-14-317-2014>, 2014.
- Barrett, E. W. and Ben-Dov, O.: Application of the Lidar to Air Pollution Measurements, *Journal of Applied Meteorology*, 6, 500–515, [https://doi.org/10.1175/1520-0450\(1967\)006<0500:AOTLTA>2.0.CO;2](https://doi.org/10.1175/1520-0450(1967)006<0500:AOTLTA>2.0.CO;2), 1967.
- Bechtold, P., Kohler, M., Jung, T., Doblas-Reyes, F., Leutbecher, M., Rodwell, M. J., Vitart, F., and Balsamo, G.: Advances in simulating atmospheric variability with the ECMWF model: From synoptic to decadal time-scales, *Quarterly Journal of the Royal Meteorological Society*, 134, 1337–1351, <https://doi.org/10.1002/qj.289>, 2008.
- Benedetti, A., Morcrette, J.-J., Boucher, O., Dethof, A., Engelen, R. J., Fisher, M., Flentje, H., Huneeus, N., Jones, L., Kaiser, J. W., Kinne, S., Mangold, A., Razinger, M., Simmons, A. J., and Suttie, M.: Aerosol analysis and forecast in the European Centre for Medium-Range Weather Forecasts Integrated Forecast System: 2. Data assimilation, *Journal of Geophysical Research: Atmospheres*, 114, <https://doi.org/10.1029/2008JD011115>, d13205, 2009.
- Binietoglou, I., Basart, S., Alados-Arboledas, L., Amiridis, V., Argyrouli, A., Baars, H., Baldasano, J. M., Balis, D., Belegante, L., Bravo-Aranda, J. A., Burlizzi, P., Carrasco, V., Chaikovsky, A., Comerón, A., D'Amico, G., Filioglou, M., Granados-Muñoz, M. J., Guerrero-Rascado, J. L., Ilic, L., Kokkalis, P., Maurizi, A., Mona, L., Monti, F., Muñoz Porcar, C., Nicolae, D., Papayannis, A., Pappalardo, G., Pejanovic, G., Pereira, S. N., Perrone, M. R., Pietruckzuk, A., Posyniak, M., Rocadenbosch, F., Rodríguez-Gómez, A., Sicard, M., Siomas, N., Szkop, A., Terradellas, E., Tsekeli, A., Vukovic, A., Wandinger, U., and Wagner, J.: A methodology for investigating dust model performance using synergistic EARLINET/AERONET dust concentration retrievals, *Atmospheric Measurement Techniques*, 8, 3577–3600, <https://doi.org/10.5194/amt-8-3577-2015>, 2015.
- Boucher, O. and Anderson, T. L.: General circulation model assessment of the sensitivity of direct climate forcing by anthropogenic sulfate aerosols to aerosol size and chemistry, *Journal of Geophysical Research: Atmospheres*, 100, 26 117–26 134, <https://doi.org/10.1029/95JD02531>, 1995.
- Boucher, O., Pham, M., and Venkataraman, C.: Simulation of the atmospheric sulfur cycle in the LMD GCM: Model description, model evaluation, and global and European budgets, *Tech. rep., Note*, 2002.
- Buizza, R., Milleer, M., and Palmer, T. N.: Stochastic representation of model uncertainties in the ECMWF ensemble prediction system, *Quarterly Journal of the Royal Meteorological Society*, 125, 2887–2908, <https://doi.org/10.1002/qj.49712556006>, 1999.
- Chan, K. L.: Biomass burning sources and their contributions to the local air quality in Hong Kong, *Science of The Total Environment*, 596–597, 212–221, <https://doi.org/https://doi.org/10.1016/j.scitotenv.2017.04.091>, 2017.



- Chan, K. L. and Chan, K. L.: Aerosol optical depths and their contributing sources in Taiwan, *Atmospheric Environment*, 148, 364–375, <https://doi.org/http://dx.doi.org/10.1016/j.atmosenv.2016.11.011>, 2017.
- Chin, M., Ginoux, P., Kinne, S., Torres, O., Holben, B. N., Duncan, B. N., Martin, R. V., Logan, J. A., Higurashi, A., and Nakajima, T.: Tropospheric Aerosol Optical Thickness from the GOCART Model and Comparisons with Satellite and Sun Photometer Measurements, 5 *Journal of the Atmospheric Sciences*, 59, 461–483, [https://doi.org/10.1175/1520-0469\(2002\)059<0461:TAOTFT>2.0.CO;2](https://doi.org/10.1175/1520-0469(2002)059<0461:TAOTFT>2.0.CO;2), 2002.
- Cuevas, E., Camino, C., Benedetti, A., Basart, S., Terradellas, E., Baldasano, J. M., Morcrette, J. J., Marticorena, B., Goloub, P., Mortier, A., Berjón, A., Hernández, Y., Gil-Ojeda, M., and Schulz, M.: The MACC-II 2007–2008 reanalysis: atmospheric dust evaluation and characterization over northern Africa and the Middle East, *Atmospheric Chemistry and Physics*, 15, 3991–4024, <https://doi.org/10.5194/acp-15-3991-2015>, 2015.
- Curci, G., Hogrefe, C., Bianconi, R., Im, U., Balzarini, A., Baró, R., Brunner, D., Forkel, R., Giordano, L., Hirtl, M., Honzak, L., Jiménez-Guerrero, P., Knote, C., Langer, M., Makar, P., Pirovano, G., Pérez, J., José, R. S., Syrakov, D., Tuccella, P., Werhahn, J., Wolke, R., Žabkar, R., Zhang, J., and Galmarini, S.: Uncertainties of simulated aerosol optical properties induced by assumptions on aerosol physical and chemical properties: An AQMEII-2 perspective, *Atmospheric Environment*, 115, 541 – 552, <https://doi.org/https://doi.org/10.1016/j.atmosenv.2014.09.009>, 2015.
- Dentener, F., Kinne, S., Bond, T., Boucher, O., Cofala, J., Generoso, S., Ginoux, P., Gong, S., Hoelzemann, J. J., Ito, A., Marelli, L., Penner, J. E., Putaud, J.-P., Textor, C., Schulz, M., van der Werf, G. R., and Wilson, J.: Emissions of primary aerosol and precursor gases in the years 2000 and 1750 prescribed data-sets for AeroCom, *Atmospheric Chemistry and Physics*, 6, 4321–4344, <https://doi.org/10.5194/acp-6-4321-2006>, 2006.
- Drusch, M., Scipal, K., de Rosnay, P., Balsamo, G., Andersson, E., Bougeault, P., and Viterbo, P.: Towards a Kalman Filter based soil moisture analysis system for the operational ECMWF Integrated Forecast System, *Geophysical Research Letters*, 36, 20 <https://doi.org/10.1029/2009GL037716>, l10401, 2009.
- Dubovik, O., Holben, B., Eck, T. F., Smirnov, A., Kaufman, Y. J., King, M. D., Tanré, D., and Slutsker, I.: Variability of absorption and optical properties of key aerosol types observed in worldwide locations, *Journal of the atmospheric sciences*, 59, 590–608, 2002.
- Dutra, E., Diamantakis, M., Tsonevsky, I., Zsoter, E., Wetterhall, F., Stockdale, T., Richardson, D., and Pappenberger, F.: The extreme forecast index at the seasonal scale, *Atmospheric Science Letters*, 14, 256–262, <https://doi.org/10.1002/asl2.448>, 2013.
- EDGAR: Emission Database for Global Atmospheric Research (EDGAR), release EDGARv4.2 FT2010, Tech. rep., European Commission, Joint Research Centre (JRC)/Netherlands Environmental Assessment Agency (PBL), 2013.
- Emeis, S., Forkel, R., Junkermann, W., Schäfer, K., Flentje, H., Gilge, S., Fricke, W., Wiegner, M., Freudenthaler, V., Groß, S., Ries, L., Meinhardt, F., Birmili, W., Münkel, C., Obleitner, F., and Suppan, P.: Measurement and simulation of the 16/17 April 2010 Eyjafjallajökull volcanic ash layer dispersion in the northern Alpine region, *Atmospheric Chemistry and Physics*, 11, 2689–2701, <https://doi.org/10.5194/acp-11-2689-2011>, 2011.
- Engelstaedter, S. and Washington, R.: Temporal controls on global dust emissions: The role of surface gustiness, *Geophysical Research Letters*, 34, <https://doi.org/10.1029/2007GL029971>, 115805, 2007.
- Fernald, F. G.: Analysis of atmospheric lidar observations: some comments, *Appl. Opt.*, 23, 652–653, <https://doi.org/10.1364/AO.23.000652>, 35 1984.
- Flentje, H., Claude, H., Elste, T., Gilge, S., Köhler, U., Plass-Dümler, C., Steinbrecht, W., Thomas, W., Werner, A., and Fricke, W.: The Eyjafjallajökull eruption in April 2010 - detection of volcanic plume using in-situ measurements, ozone sondes and lidar-ceilometer profiles, *Atmospheric Chemistry and Physics*, 10, 10 085–10 092, <https://doi.org/10.5194/acp-10-10085-2010>, 2010.



- Geisinger, A., Behrendt, A., Wulfmeyer, V., Strohbach, J., Förstner, J., and Potthast, R.: Development and application of a backscatter lidar forward operator for quantitative validation of aerosol dispersion models and future data assimilation, *Atmospheric Measurement Techniques*, 10, 4705–4726, <https://doi.org/10.5194/amt-10-4705-2017>, 2017.
- Groß, S., Freudenthaler, V., Schepanski, K., Toledano, C., Schäfler, A., Ansmann, A., and Weinzierl, B.: Optical properties of long-range transported Saharan dust over Barbados as measured by dual-wavelength depolarization Raman lidar measurements, *Atmospheric Chemistry and Physics*, 15, 11 067–11 080, <https://doi.org/10.5194/acp-15-11067-2015>, 2015.
- 5 Guelle, W., Balkanski, Y. J., Schulz, M., Marticorena, B., Bergametti, G., Moulin, C., Arimoto, R., and Perry, K. D.: Modeling the atmospheric distribution of mineral aerosol: Comparison with ground measurements and satellite observations for yearly and synoptic timescales over the North Atlantic, *Journal of Geophysical Research: Atmospheres*, 105, 1997–2012, <https://doi.org/10.1029/1999JD901084>, 2000.
- Hess, M., Koepke, P., and Schult, I.: Optical properties of aerosols and clouds: The software package OPAC, *Bulletin of the American meteorological society*, 79, 8–844, 1998.
- IPCC: IPCC, 2012: Managing the Risks of Extreme Events and Disasters to Advance Climate Change Adaptation. A Special Report of Working Groups I and II of the Intergovernmental Panel on Climate Change, Cambridge University Press, Cambridge, UK, and New York, NY, USA, 2012.
- Jones, A., Roberts, D. L., Woodage, M. J., and Johnson, C. E.: Indirect sulphate aerosol forcing in a climate model with an interactive sulphur cycle, *Journal of Geophysical Research: Atmospheres*, 106, 20 293–20 310, <https://doi.org/10.1029/2000JD000089>, 2001.
- Kalnay, E., Kanamitsu, M., Kistler, R., Collins, W., Deaven, D., Gandin, L., Iredell, M., Saha, S., White, G., Woollen, J., et al.: The NCEP/NCAR 40-year reanalysis project, *Bulletin of the American meteorological Society*, 77, 437–471, 1996.
- 20 Kandler, K., Schütz, L., Deutscher, C., Ebert, M., Hofmann, H., Jäckel, S., Jaenicke, R., Knippertz, P., Lieke, K., Massling, A., Petzold, A., Schladitz, A., Weinzierl, B., Wiedensohler, A., Zorn, S., and Weinbruch, S.: Size distribution, mass concentration, chemical and mineralogical composition and derived optical parameters of the boundary layer aerosol at Tinfou, Morocco, during SAMUM 2006, *Tellus B*, 61, 32–50, <https://doi.org/10.1111/j.1600-0889.2008.00385.x>, 2009.
- Kazil, J., Stier, P., Zhang, K., Quaas, J., Kinne, S., O'Donnell, D., Rast, S., Esch, M., Ferrachat, S., Lohmann, U., and Feichter, J.: Aerosol nucleation and its role for clouds and Earth's radiative forcing in the aerosol-climate model ECHAM5-HAM, *Atmospheric Chemistry and Physics*, 10, 10 733–10 752, <https://doi.org/10.5194/acp-10-10733-2010>, 2010.
- Klett, J. D.: Stable analytical inversion solution for processing lidar returns, *Appl. Opt.*, 20, 211–220, <https://doi.org/10.1364/AO.20.000211>, 1981.
- Köpke, P., Hess, M., Schult, I., and Shettle, E.: Global aerosol data set, Max-Planck-Institut für Meteorologie Hamburg, Germany, 1997.
- 25 Lohmann, U., Stier, P., Hoose, C., Ferrachat, S., Kloster, S., Roeckner, E., and Zhang, J.: Cloud microphysics and aerosol indirect effects in the global climate model ECHAM5-HAM, *Atmospheric Chemistry and Physics*, 7, 3425–3446, <https://doi.org/10.5194/acp-7-3425-2007>, 2007.
- Madonna, F., Amato, F., Vande Hey, J., and Pappalardo, G.: Ceilometer aerosol profiling versus Raman lidar in the frame of the INTERACT campaign of ACTRIS, *Atmospheric Measurement Techniques*, 8, 2207–2223, <https://doi.org/10.5194/amt-8-2207-2015>, 2015.
- 30 Mann, G. W., Carslaw, K. S., Ridley, D. A., Spracklen, D. V., Pringle, K. J., Merikanto, J., Korhonen, H., Schwarz, J. P., Lee, L. A., Manktelow, P. T., Woodhouse, M. T., Schmidt, A., Breider, T. J., Emmerson, K. M., Reddington, C. L., Chipperfield, M. P., and Pickering, S. J.: Intercomparison of modal and sectional aerosol microphysics representations within the same 3-D global chemical transport model, *Atmospheric Chemistry and Physics*, 12, 4449–4476, <https://doi.org/10.5194/acp-12-4449-2012>, 2012.



Mishchenko, M. I. and Travis, L. D.: Capabilities and limitations of a current FORTRAN implementation of the T-matrix method for randomly oriented, rotationally symmetric scatterers, *Journal of Quantitative Spectroscopy and Radiative Transfer*, 60, 309–324, [https://doi.org/https://doi.org/10.1016/S0022-4073\(98\)00008-9](https://doi.org/https://doi.org/10.1016/S0022-4073(98)00008-9), 1998.

Mishchenko, M. I., Dlugach, J. M., Yanovitskij, E. G., and Zakharova, N. T.: Bidirectional reflectance of flat, optically thick particulate layers:
5 an efficient radiative transfer solution and applications to snow and soil surfaces, *Journal of Quantitative Spectroscopy and Radiative Transfer*, 63, 409–432, [https://doi.org/http://dx.doi.org/10.1016/S0022-4073\(99\)00028-X](https://doi.org/http://dx.doi.org/10.1016/S0022-4073(99)00028-X), 1999.

Morcrette, J.-J., Beljaars, A., Benedetti, A., Jones, L., and Boucher, O.: Sea-salt and dust aerosols in the ECMWF IFS model, *Geophysical Research Letters*, 35, <https://doi.org/10.1029/2008GL036041>, l24813, 2008.

Morcrette, J.-J., Boucher, O., Jones, L., Salmond, D., Bechtold, P., Beljaars, A., Benedetti, A., Bonet, A., Kaiser, J. W., Razinger, M.,
10 Schulz, M., Serrar, S., Simmons, A. J., Sofiev, M., Suttie, M., Tompkins, A. M., and Untch, A.: Aerosol analysis and forecast in the European Centre for Medium-Range Weather Forecasts Integrated Forecast System: Forward modeling, *Journal of Geophysical Research: Atmospheres*, 114, <https://doi.org/10.1029/2008JD011235>, d06206, 2009.

Müller, D., Heinold, B., Tesche, M., Tegen, I., Althausen, D., Arboledas, L. A., Amiridis, V., Amodeo, A., Ansmann, A., Balis, D., Comeron, A., D'amico, G., Gerasopoulos, E., Guerrero-Rascado, J. L., Freudenthaler, V., Giannakaki, E., Heese, B., Iarlori, M., Knippertz, P.,
15 Mamouri, R. E., Mona, L., Papayannis, A., Pappalardo, G., Perrone, R.-M., Pisani, G., Rizi, V., Sicard, M., Spinelli, N., Tafuro, A., and Wiegner, M.: EARLINET observations of the 14–22 May long-range dust transport event during SAMUM 2006: validation of results from dust transport modelling, *Tellus B*, 61, 325–339, <https://doi.org/10.1111/j.1600-0889.2008.00400.x>, 2009.

O'Dowd, C. D., Lowe, J. A., Smith, M. H., Davison, B., Hewitt, C. N., and Harrison, R. M.: Biogenic sulphur emissions and inferred non-sea-salt-sulphate cloud condensation nuclei in and around Antarctica, *Journal of Geophysical Research: Atmospheres*, 102, 12 839–12 854,
20 <https://doi.org/10.1029/96JD02749>, 1997.

Rabier, F., Jarvinen, H., Klinker, E., Mahfouf, J.-F., and Simmons, A.: The ECMWF operational implementation of four-dimensional variational assimilation. I: Experimental results with simplified physics, *Quarterly Journal of the Royal Meteorological Society*, 126, 1143–1170, <https://doi.org/10.1002/qj.49712656415>, 2000.

Reddy, M. S., Boucher, O., Bellouin, N., Schulz, M., Balkanski, Y., Dufresne, J.-L., and Pham, M.: Estimates of global multicomponent
25 aerosol optical depth and direct radiative perturbation in the Laboratoire de Meteorologie Dynamique general circulation model, *Journal of Geophysical Research: Atmospheres*, 110, <https://doi.org/10.1029/2004JD004757>, d10S16, 2005.

Shettle, E. P. and Fenn, R. W.: Models for the aerosols of the lower atmosphere and the effects of humidity variations on their optical properties, *Tech. Rep. Environmental research papers No. 675*, NTIS, ADA 085951, AFGL-TR-79-0214, Air Force Geophysics Lab Hanscom Afb Ma, 1979.

Siomos, N., Balis, D. S., Poupkou, A., Liora, N., Dimopoulos, S., Melas, D., Giannakaki, E., Filioglou, M., Basart, S., and Chaikovsky, A.: Investigating the quality of modeled aerosol profiles based on combined lidar and sunphotometer data, *Atmospheric Chemistry and Physics*, 17, 7003–7023, <https://doi.org/10.5194/acp-17-7003-2017>, 2017.

Stier, P., Feichter, J., Kinne, S., Kloster, S., Vignati, E., Wilson, J., Ganzeveld, L., Tegen, I., Werner, M., Balkanski, Y., Schulz, M., Boucher, O., Minikin, A., and Petzold, A.: The aerosol-climate model ECHAM5-HAM, *Atmospheric Chemistry and Physics*, 5, 1125–0156,
35 <https://doi.org/10.5194/acp-5-1125-2005>, 2005.

Stuut, J.-B., Smalley, I., and O'Hara-Dhand, K.: Aeolian dust in Europe: African sources and European deposits, *Quaternary International*, 198, 234–245, <https://doi.org/http://dx.doi.org/10.1016/j.quaint.2008.10.007>, loess in the Danube Region and Surrounding Loess Provinces: The Marsigli Memorial Volume, 2009.



Swietlicki, E., Hansson, H.-C., Hämeri, K., Svenningsson, B., Massling, A., McFiggans, G., McMurry, P. H., Petäjä, T., Tunved, P., Gysel, M., Topping, D., Weingartner, E., Baltensperger, U., Rissler, J., Wiedensohler, A., and Kulmala, M.: Hygroscopic properties of submicrometer atmospheric aerosol particles measured with H-TDMA instruments in various environments — a review, Tellus B, 60, 432–469, <https://doi.org/10.1111/j.1600-0889.2008.00350.x>, 2008.

- 5 van der Werf, G. R., Randerson, J. T., Giglio, L., Collatz, G. J., Mu, M., Kasibhatla, P. S., Morton, D. C., DeFries, R. S., Jin, Y., and van Leeuwen, T. T.: Global fire emissions and the contribution of deforestation, savanna, forest, agricultural, and peat fires (1997–2009), Atmospheric Chemistry and Physics, 10, 11 707–11 735, <https://doi.org/10.5194/acp-10-11707-2010>, 2010.
- Wang, M., Ghan, S., Ovchinnikov, M., Liu, X., Easter, R., Kassianov, E., Qian, Y., and Morrison, H.: Aerosol indirect effects in a multi-scale aerosol-climate model PNNL-MMF, Atmospheric Chemistry and Physics, 11, 5431–5455, <https://doi.org/10.5194/acp-11-5431-2011>,
10 2011.
- Wang, Y., Sartelet, K. N., Bocquet, M., Chazette, P., Sicard, M., D'Amico, G., Léon, J. F., Alados-Arboledas, L., Amodeo, A., Augustin, P., Bach, J., Belegante, L., Binetoglou, I., Bush, X., Comerón, A., Delbarre, H., García-Vázquez, D., Guerrero-Rascado, J. L., Hervo, M., Iarlori, M., Kokkalis, P., Lange, D., Molero, F., Montoux, N., Muñoz, A., Muñoz, C., Nicolae, D., Papayannis, A., Pappalardo, G., Preissler, J., Rizi, V., Rocadenbosch, F., Sellegri, K., Wagner, F., and Dulac, F.: Assimilation of lidar signals: application to aerosol forecasting in the
15 western Mediterranean basin, Atmospheric Chemistry and Physics, 14, 12 031–12 053, <https://doi.org/10.5194/acp-14-12031-2014>, 2014.
- Waterman, P. C.: Symmetry, Unitarity, and Geometry in Electromagnetic Scattering, Phys. Rev. D, 3, 825–839,
20 <https://doi.org/10.1103/PhysRevD.3.825>, 1971.
- Wiegner, M. and Gasteiger, J.: Correction of water vapor absorption for aerosol remote sensing with ceilometers, Atmospheric Measurement Techniques, 8, 3971–3984, <https://doi.org/10.5194/amt-8-3971-2015>, 2015.
- 20 Wiegner, M. and Geiß, A.: Aerosol profiling with the Jenoptik ceilometer CHM15kx, Atmospheric Measurement Techniques, 5, 1953–1964,
<https://doi.org/10.5194/amt-5-1953-2012>, 2012.
- Wiegner, M., Gasteiger, J., Kandler, K., Weinzierl, B., Rasp, K., Eselborn, M., Freudenthaler, V., Heese, B., Toledano, C., Tesche, M., and
25 Althausen, D.: Numerical simulations of optical properties of Saharan dust aerosols with emphasis on lidar applications, Tellus B, 61, 180–194, <https://doi.org/10.1111/j.1600-0889.2008.00381.x>, 2009.
- Wiegner, M., Madonna, F., Binetoglou, I., Forkel, R., Gasteiger, J., Geiß, A., Pappalardo, G., Schäfer, K., and Thomas, W.: What is the
30 benefit of ceilometers for aerosol remote sensing? An answer from EARLINET, Atmospheric Measurement Techniques, 7, 1979–1997,
<https://doi.org/10.5194/amt-7-1979-2014>, 2014.
- Zhang, K., O'Donnell, D., Kazil, J., Stier, P., Kinne, S., Lohmann, U., Ferrachat, S., Croft, B., Quaas, J., Wan, H., Rast, S., and Feichter,
J.: The global aerosol-climate model ECHAM-HAM, version 2: sensitivity to improvements in process representations, Atmospheric
Chemistry and Physics, 12, 8911–8949, <https://doi.org/10.5194/acp-12-8911-2012>, 2012.
- Zhang, Y., Seigneur, C., Seinfeld, J. H., Jacobson, M. Z., and Binkowski, F. S.: Simulation of Aerosol Dynamics: A Comparative Review of
Algorithms Used in Air Quality Models, Aerosol Science and Technology, 31, 487–514, <https://doi.org/10.1080/027868299304039>, 1999.
- Zieger, P., Fierz-Schmidhauser, R., Weingartner, E., and Baltensperger, U.: Effects of relative humidity on aerosol light scattering: results
from different European sites, Atmospheric Chemistry and Physics, 13, 10 609–10 631, <https://doi.org/10.5194/acp-13-10609-2013>, 2013.

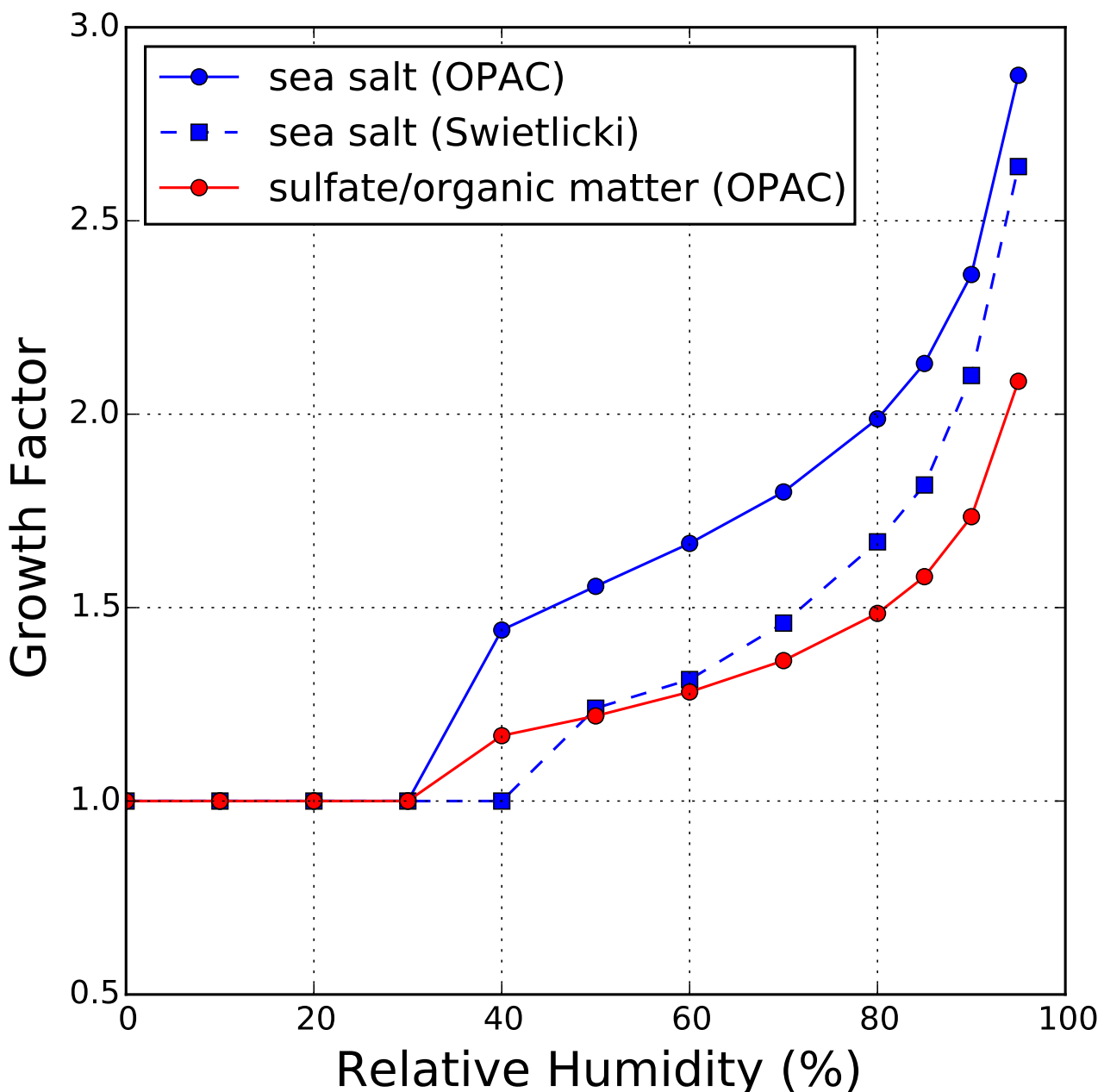


Figure 1. Hygroscopic growth factors of particle radius of sea salt, sulfate and hydrophilic organic matter aerosols as a function of relative humidity. Sulfate and hydrophilic organic matter share the same growth factor in the model (red curve). Growth factors of sea salt obtained from Swietlicki et al. (2008) are also shown for reference.

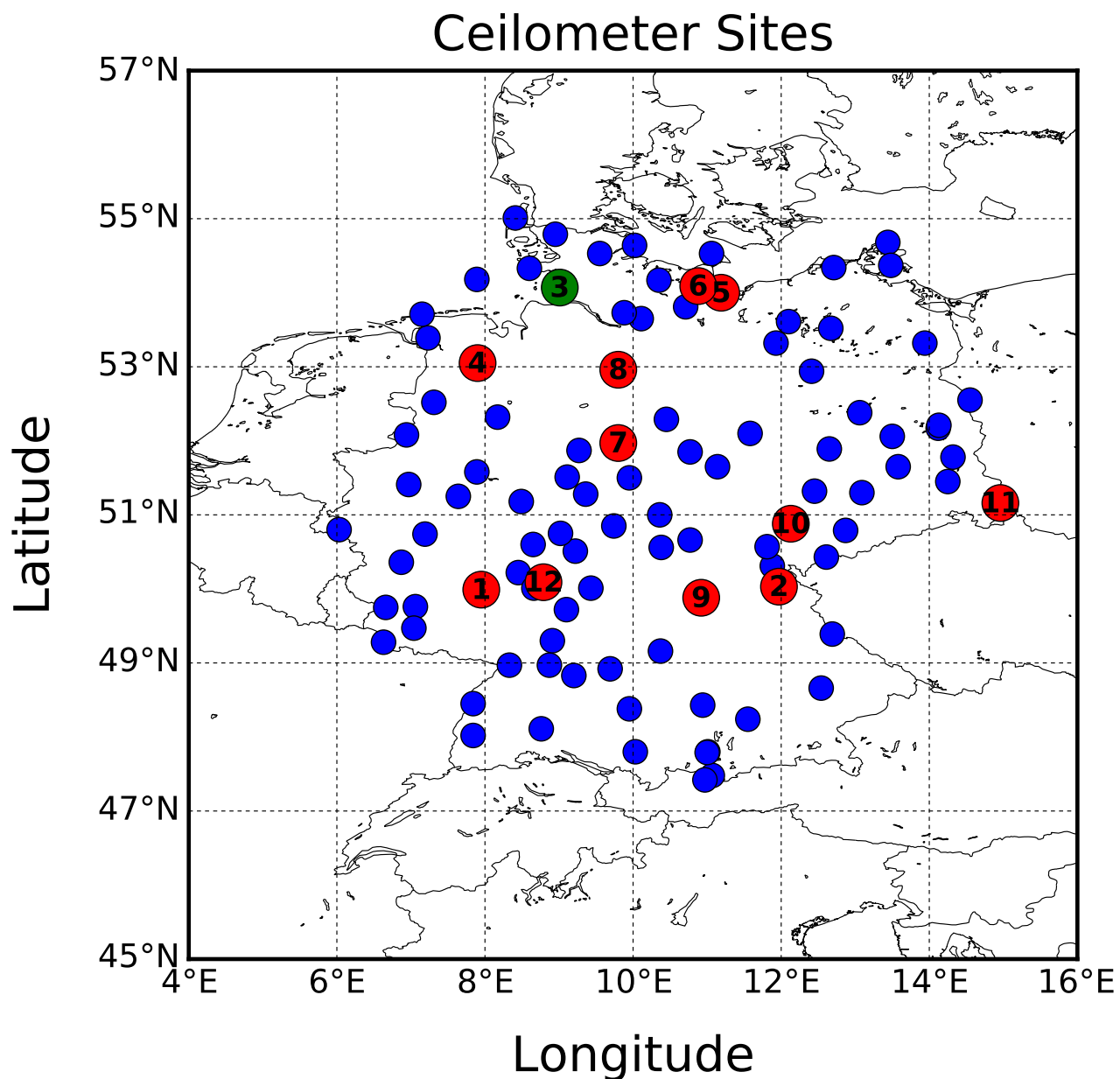


Figure 2. Location of the German weather service ceilometer sites as on end of 2017. The red spots indicate the ceilometer sites within 20 km of IFS model grid point while the blue markers represent the rest of the network. Note that some of the sites are not in operation during the period of study and therefore not included in this study. Elpersbüttel (see section 4) is indicated in green. More detailed information of the ceilometer sites can be found in Table 1.

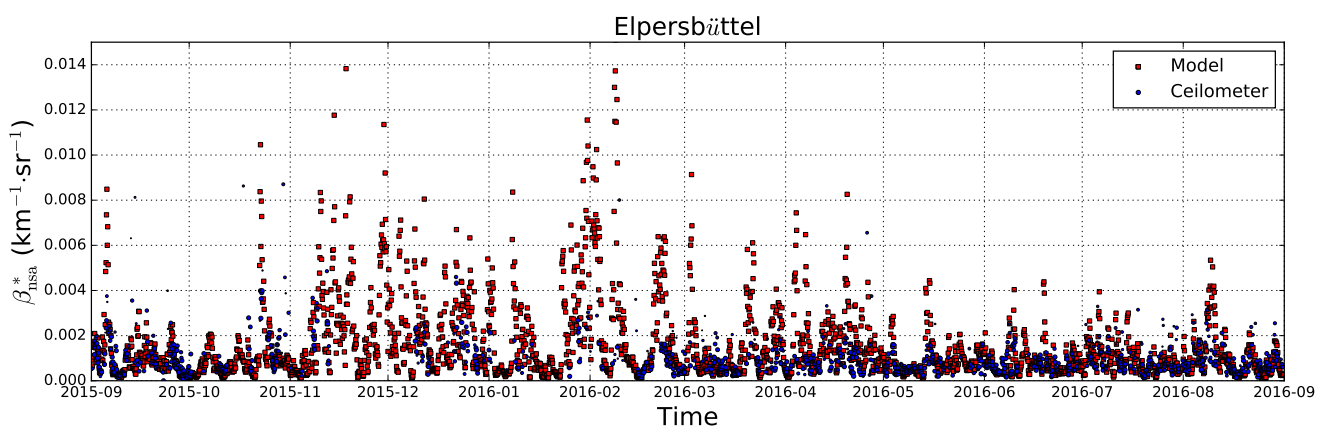


Figure 3. Time series (from 1. September 2015 to 31. August 2016) of the model simulation and ceilometer observation of near surface attenuated backscatter $\overline{\beta_{ns}^*}$ in $\text{km}^{-1} \text{sr}^{-1}$ over Elpersbüttel with $\overline{\beta_{ns}^*}$ being averaged from 200 m ("full overlap height") up to 1 km above ground.

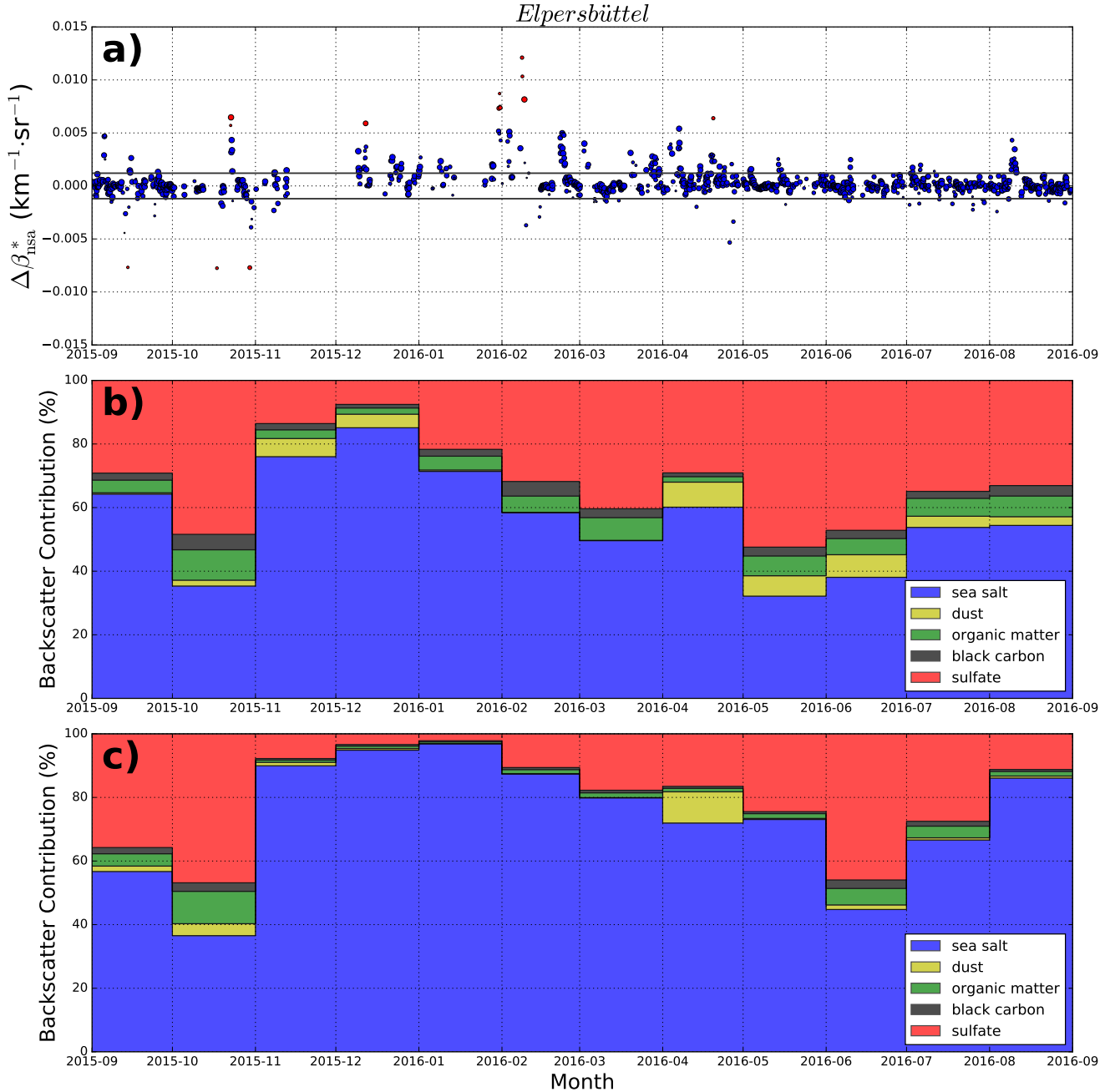


Figure 4. (a) Differences Δ of near surface attenuated backscatter $\overline{\beta}_{ns}^*$ for Elpersbüttel according to Eq. 12. The horizontal line indicates the standard deviation σ of the differences. The size of the markers represents the number of ceilometer measurements available for each individual comparison. Differences $\Delta > 3\sigma$ are shown in red. (b) Contribution of different aerosol types to $\overline{\beta}_{ns}^*$ for cases with $\Delta < \sigma$. (c) same as (b) but cases with $\Delta > \sigma$.

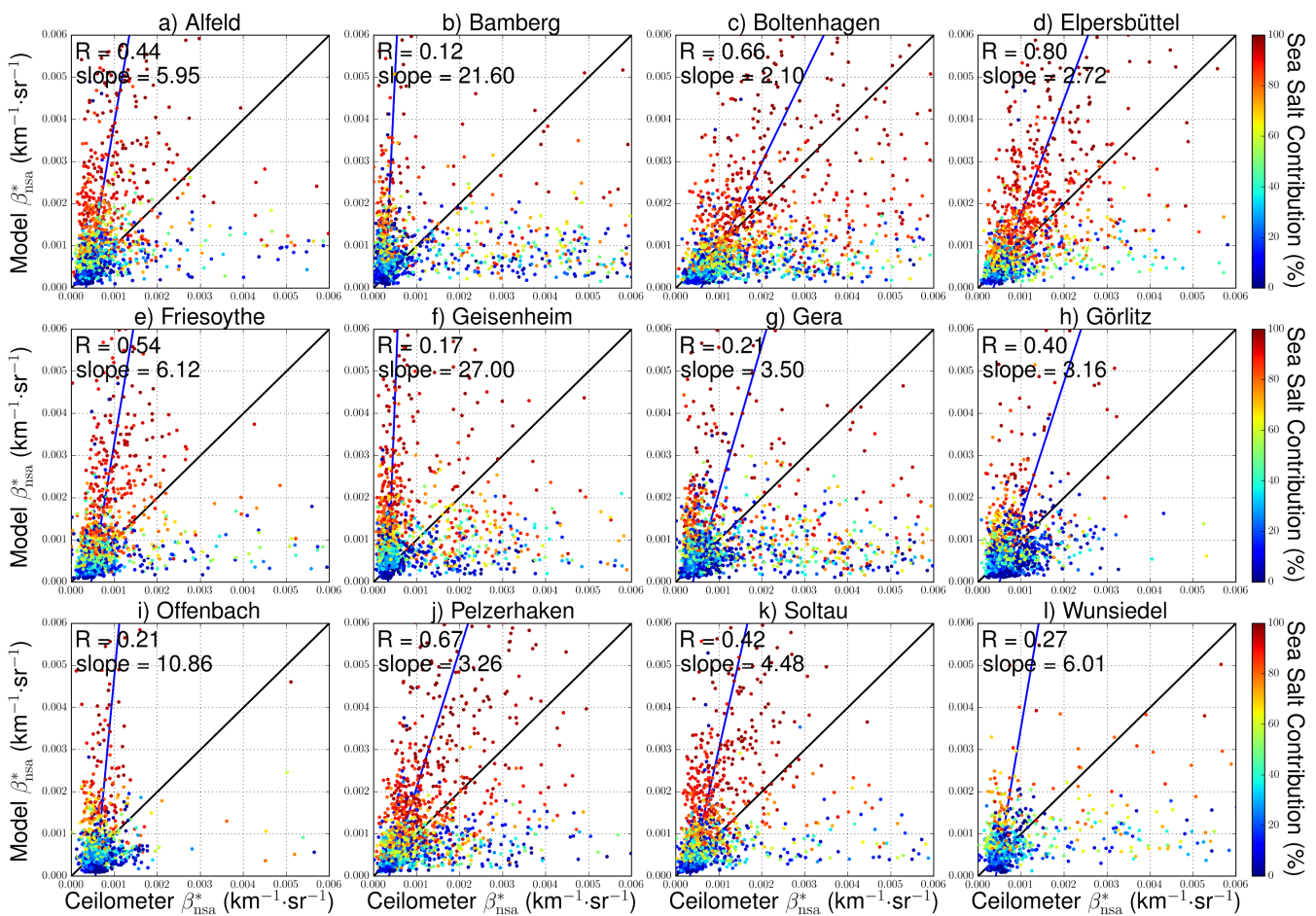


Figure 5. Scatter plots of ceilometer derived and modeled $\overline{\beta_{nsa}^*}$ for the 12 sites listed in Table 1. The color code represents the relative contribution of sea salt to $\overline{\beta_{nsa}^*}$. The blue curve indicates the total least squares regression line of the data points with at least 120 ceilometer profiles, while the black line represents the 1 to 1 reference.

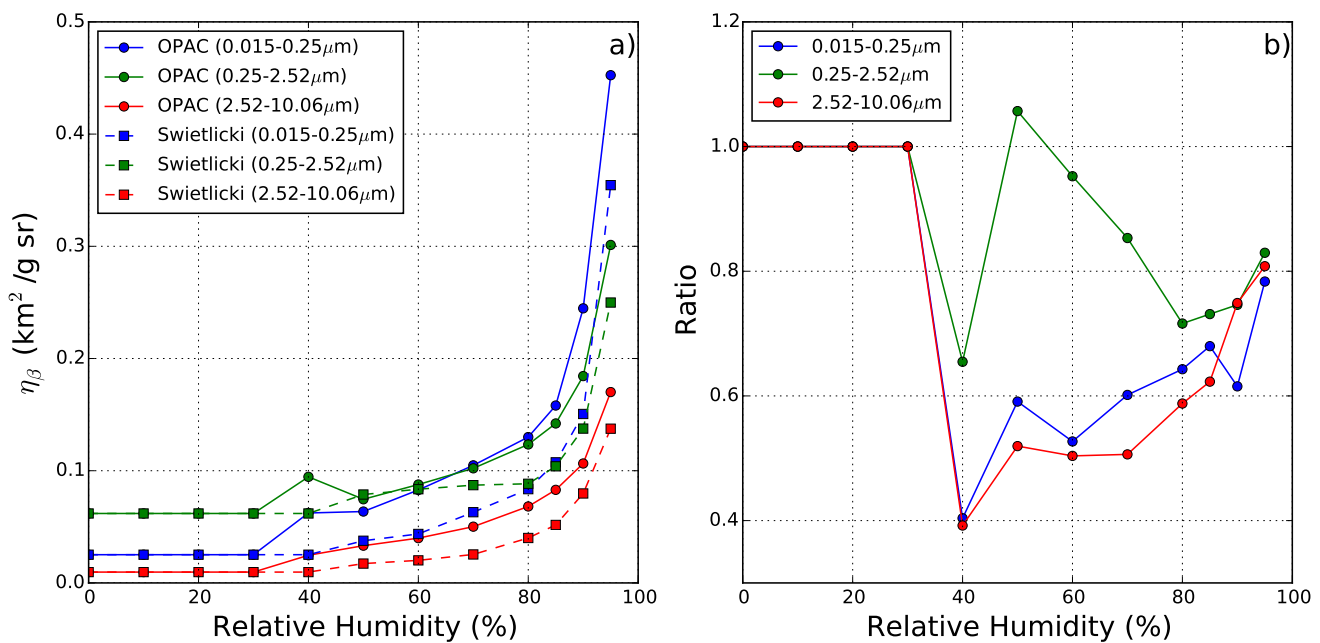


Figure 6. a) Mass mixing ratio to backscatter coefficient conversion factors $\eta_{\beta,i}$ of sea salt aerosol for the three small, medium and large size bin (in blue, green and red) at different ambient relative humidities. Hygroscopic growth factors of sea salt are taken from the model assumption (solid circle curve) and Swietlicki et al. (2008) (dashed square curve). The ratio of mass mixing ratio to backscatter coefficient conversion factors between the hygroscopic growth effects taken from Swietlicki et al. (2008) and OPAC databases are shown in b), ratios smaller than 1 indicate a reduction when using hygroscopic growth from Swietlicki et al. (2008).

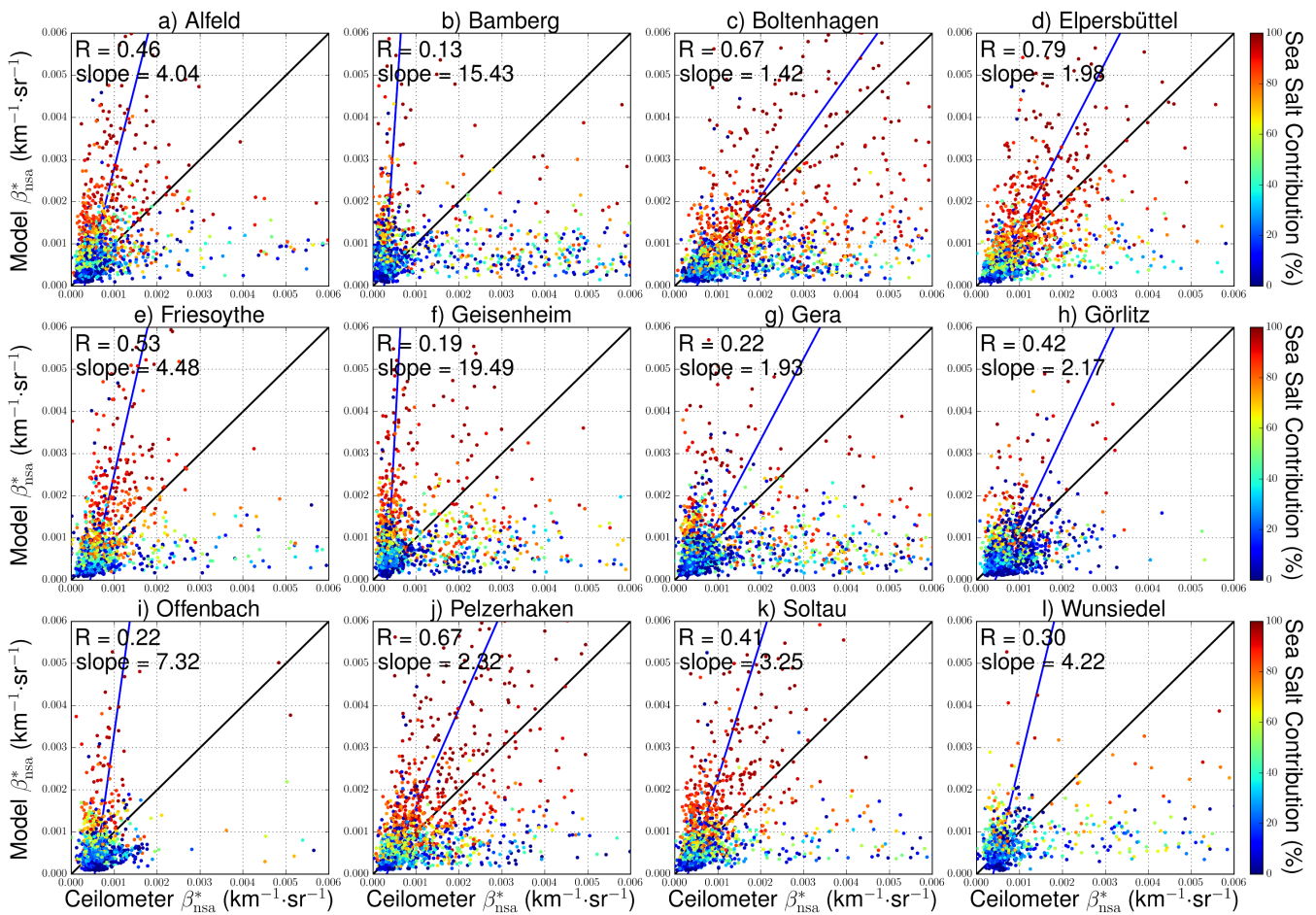


Figure 7. Scatter plots of the ceilometer and model surface attenuated backscatter signals for the 12 sites listed in Table 1. Model data are converted to attenuated backscatter signal based on hygroscopic growth factors introduced in Swietlicki et al. (2008). Color code represents the relative contribution of sea salt to backscatter signal. The blue curve indicates the total least squares regression line of data point with at least 120 ceilometer profiles, while the black curve represents the 1 to 1 reference.

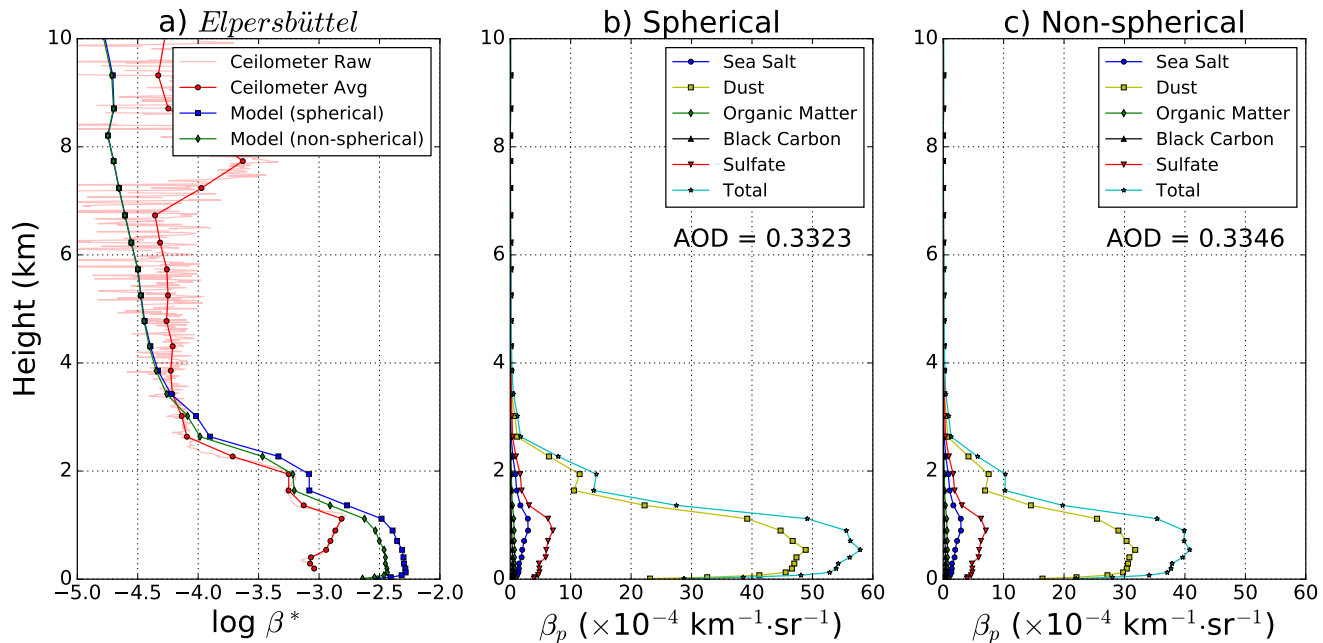


Figure 8. (a) Attenuated backscatter derived from the IFS-model and the ceilometer data, respectively, during a dust episode at 18:00 UTC on 3. April 2016 in Elpersbüttel. Model data are converted to β^* assuming either spherical (blue curve) and non-spherical (green curve) dust particles. Model results of the particle backscatter coefficient β_p (light green) together with the contributions of each aerosol type assuming either spherical (b) or non-spherical (c) particle shape. The aerosol optical depth at 1064 nm is virtually the same ($\text{AOD} \approx 0.33$)

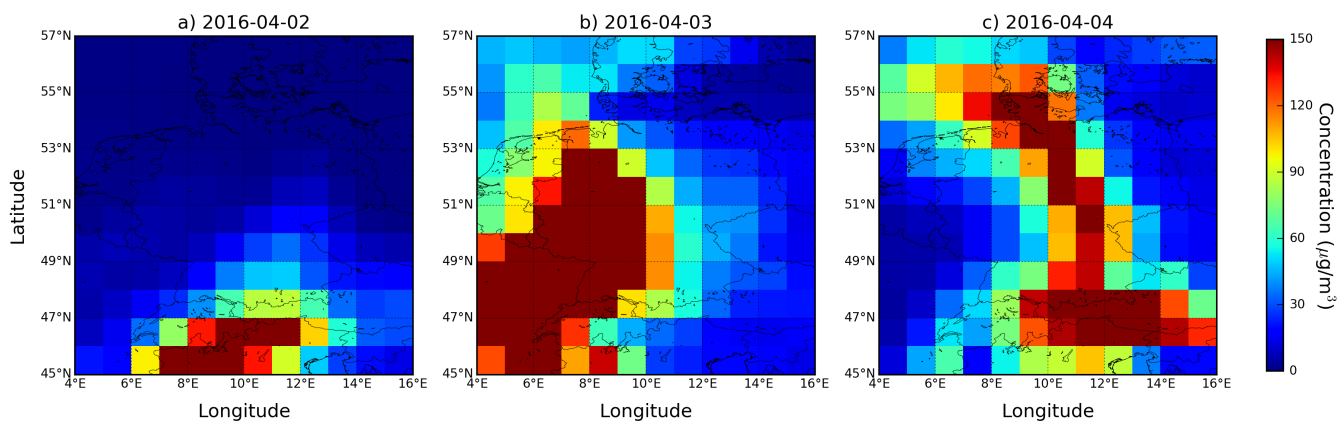


Figure 9. Dust concentration (averaged over the lowermost kilometer of the troposphere, in $\mu\text{g}/\text{m}^3$) over Germany as predicted from the IFS-model: 2. April to 4. April 2016 (from left to right), 12:00 UTC

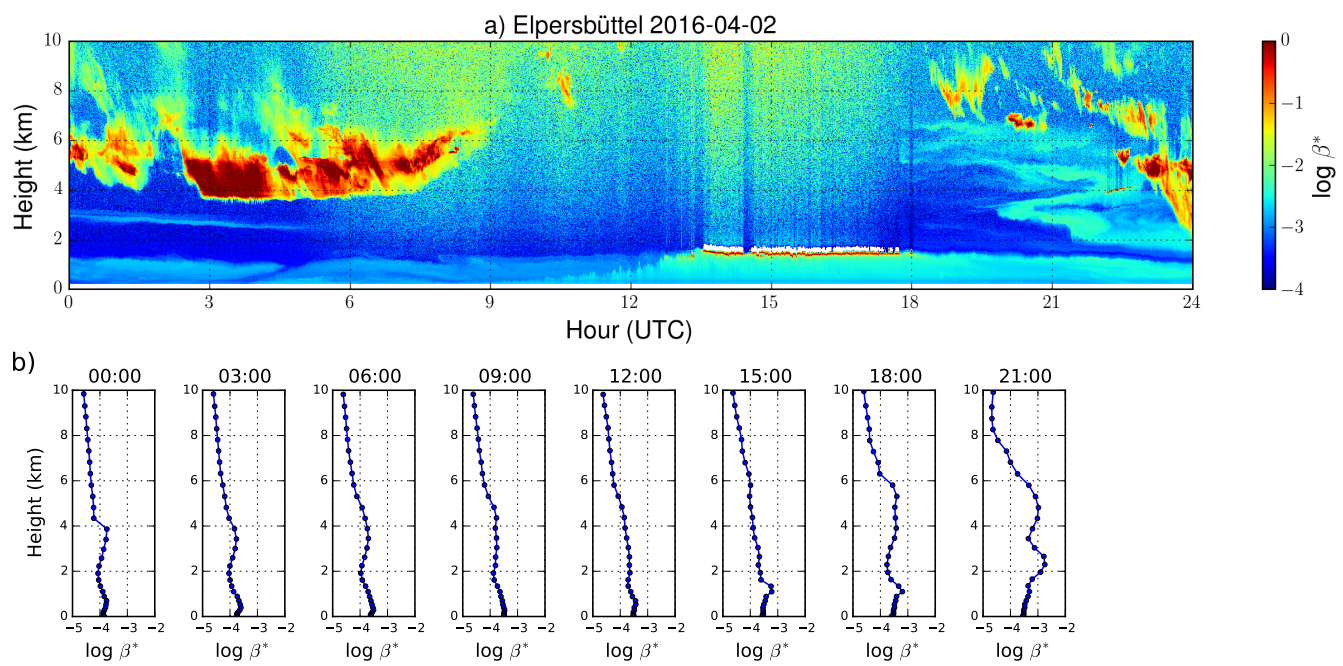


Figure 10. Time series of attenuated backscatter measured by the ceilometer (upper panel) and simulated by the model (lower panel) at Elpersbüttel during a dust episode on 2. April 2016.

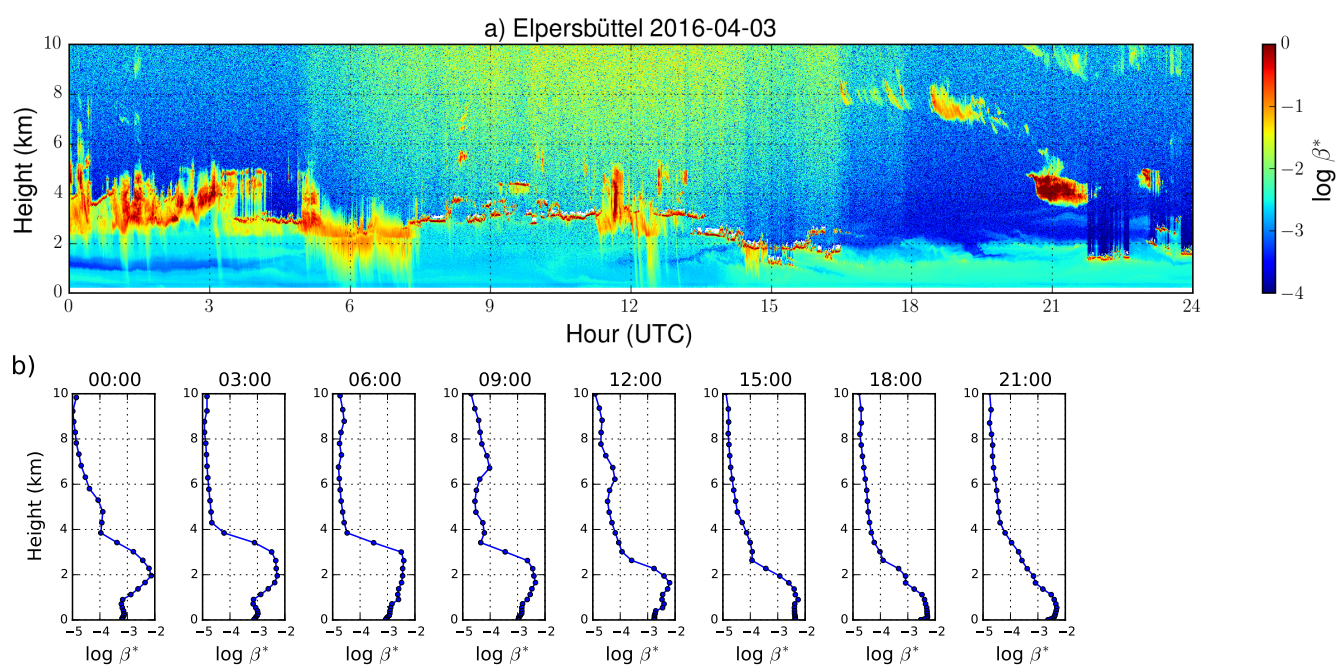


Figure 11. Same as Fig. 10 but 3. April 2016.

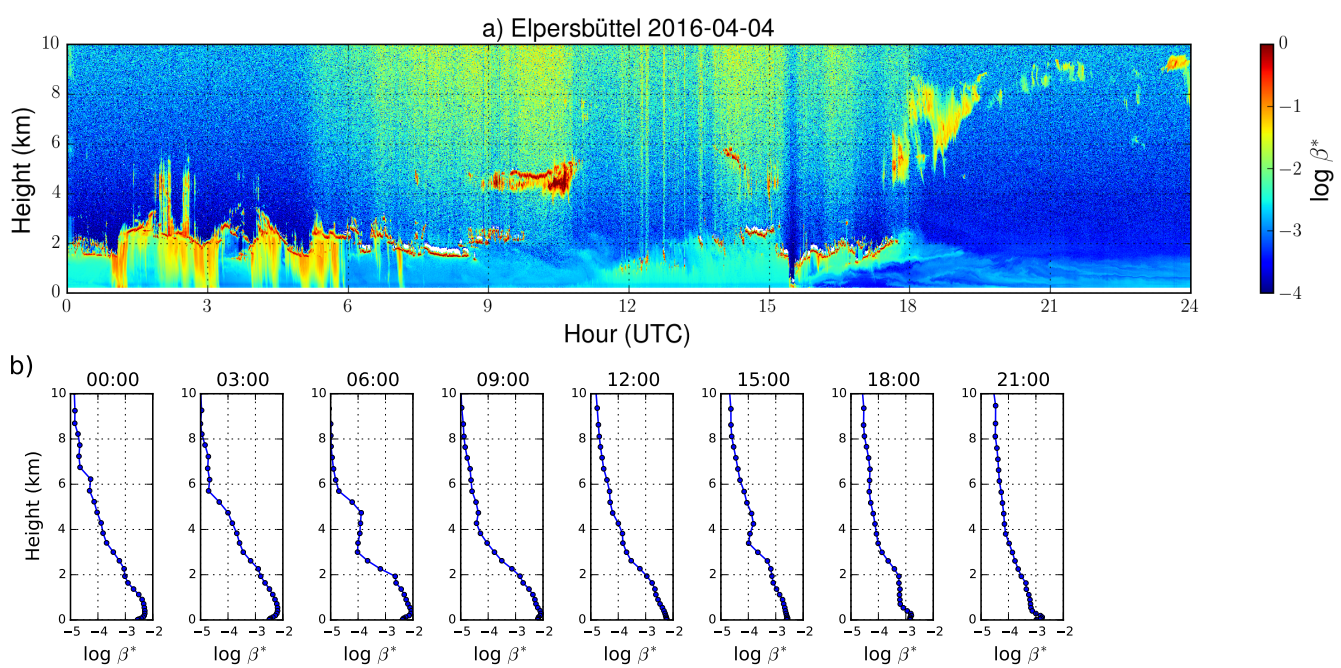


Figure 12. same as Fig. 10 but for 4. April 2016.